AN ABSTRACT OF THE THESIS OF

Miguel Soler for the degree of Master of Science in Mechanical Engineering presented on December 7, 2016.

Title: Computational Investigation on the Effects of Arc Location in Vacuum Arc Remelting

Abstract approved: _____

Kyle E Niemeyer

Vacuum arc remelting (VAR) is a secondary melting process for exotic alloys. The main purpose of this process is to increase the input ingot's physical and chemical homogeneity. This is accomplished through the application of a high current that melts the material through the emergence of electrical arcs that induce Joule heating. Arc behavior drives quality of the end product, but no methodology is currently used in VAR furnaces at large scale to track arcs in real time. An arc position sensing (APS) technology was recently developed as a way to predict arc locations using magnetic field values measured by sensors. This system couples finite element analysis of VAR furnace magnetostatics with direct magnetic field measurements to predict arc locations. Vertical position of the sensor relative to the electrode-ingot gap, a varying electrode-ingot gap size, ingot shrink-age, and the use of multiple sensors rather than a single sensor were studied to analyze potential changes of previous made assumptions and their effects on arc location prediction accuracy. Among the parameters studied, only vertical distance between arc and sensor locations causes large sources of error, and should be considered further when applying an APS system. However, averaging the predicted locations from four evenly spaced sensors helps reduce this error. In addition, the effects of the arc position on the solidification of the ingot was also studied. Where the arc is located alters the heat transfer and fluid dynamics of the liquid melt pool. Being able to both locate and conclude how exactly arc position effects the final product could aid in the development of arc position sensing technology and the industry as a whole.

Computational Investigation on the Effects of Arc Location in Vacuum Arc Remelting

by

Miguel Soler

A THESIS

submitted to

Oregon State University

in partial fulfillment of
the requirements for the
degree of

Master of Science

Presented December 7, 2016
Commencement June 2017

Master of Science thesis of Miguel Soler presented on December 7, 2016.

APPROVED:

Major Professor, representing Mechanical Engineering

Head of the School of Mechanical, Industrial, and Manufacturing Engineering

---

Dean of the Graduate School

I understand that my thesis will become part of the permanent collection of Oregon State University libraries. My signature below authorizes release of my thesis to any reader upon request.

Miguel Soler, Author

ACKNOWLEDGEMENTS

This material is based on work supported by Oregon BEST under grant reference number "CG-SOW-2015-OSU-KW Associates". I would like to thank Paul King, Rigel Woodside, and Matt Cibula of KW Associates LLC for helpful discussions and comments on the work presented on this thesis.

I would like to thank my advisor, Dr. Niemeyer, for his guidance, knowledge, and help he has provided me. For giving me the opportunity to work on this project, and more importantly for being a role model and leader that I can look up to.

Thanks to everyone in the Niemeyer research group, for being exemplary colleagues and friends.

I would like to thank Lynn Paul, for believing in me and convincing me to continue my education through the pursuit of this degree.

I would like to thank my family, for their tremendous support. For instilling the importance and value of education, to always look back to where you come from, and to strive to be a better person every day. I would not be here without them.

TABLE OF CONTENTS

LIST OF FIGURES

LIST OF FIGURES (Continued)

Figure Page

LIST OF TABLES

Chapter 1: Introduction

1.1 Vacuum arc remelting

Vacuum arc remelting, or VAR, is a secondary melting process for metal alloys, which include titanium, nickel, zirconium, and niobium alloys. The main purpose of this casting process is to increase the input ingot's homogeneity, both in crystalline structure and macrostructure. Metal ingots that exhibit higher homogeneity offer consistent material properties from all directions without irregularities. This attribute presents advantages towards the use of these metals in demanding applications such as aerospace systems, where the material will be under high temperature and structural stresses over many cycles. Products that incorporate metals processed through VAR systems can be found in everyday environments. In addition to aerospace applications, VAR-processed alloys can be found in chemical, energy, food process, marine, military, and many more industries. The VAR industry is a multi-billion dollar industry with roots in the state of Oregon, where the technology was developed in its infancy [15]. Oregon still hosts many corporations that specialize in the process such as ATI and Precision Cast Parts.

The VAR process is driven by the input of high electrical currents that create high heat transfer in the form of joule heating to melt an input specimen, or the electrode. This all occurs in a vacuum chamber. The currents form electrical arcs in between the electrode and the resultant ingot. These arcs are a key parameter of the process. The input material melts and mass drops via gravity to the crucible. Crucibles are usually made out of copper and water cooled. Figure 1.1 shows a detailed diagram of a VAR furnace. Ingots will undergo the VAR process multiple times until the desired characteristics are achieved, then they can be prepared to be made into their final parts.

Due to VAR processed alloys being employed in extreme conditions, even one minor imperfection can result in catastrophic consequences. For this reason it is crucial to attempt to study the process as much as possible.

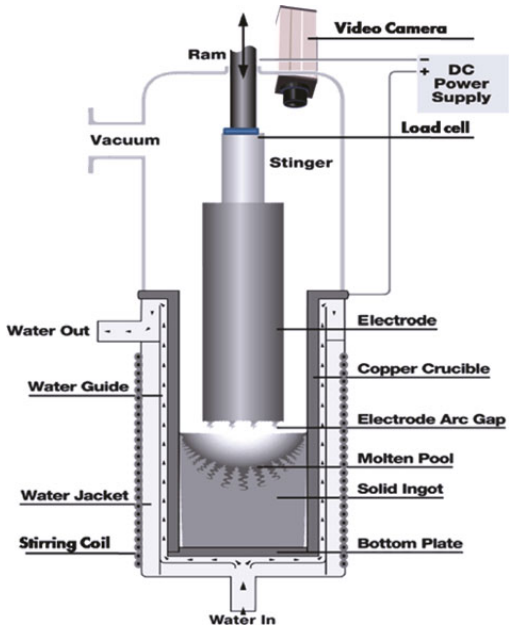

Figure 1.1: Cross section of VAR furnace. Image taken from Woodside et al. [15]

1.2 Motivation

The electrical arcs that that form during vacuum arc remelting are the most important aspect of the process. Arc movement and location directly influences the solidification of the ingot, and in turn, the quality of the final product. For being such an integral part of the system, operators do not have access to technology to track arcs during the process, or a perfect understanding on arc behavior and its correlation to the formation of imperfections on ingots. Therefore, in order to improve vacuum arc remelting efficiency and knowledge, the work on this thesis focuses on the following objectives:

1. The numerical study on an arc position sensing technology's sensitivity to parameters that were initially overlooked.

2. The building of the foundation for a solidification model that can correlate arc position to solidification characteristics.

Currently VAR furnaces are operated by pre-assigning a specified melt rate depending on the electrode in question. The controls system of the VAR will attempt to keep the

melt rate steady by using the weight of the ingot to approximate the progress of the melt. The arcs that form in the electrode-ingot gap are crucial to the final products characteristics. There is currently no widespread use of a technology that can detect or measure arcs in real time. This results in wasted energy and wasted material if imperfections are found later, and imperfections that fail to be identified on these parts could cost corporations drastically due to where VAR-processed alloys are employed. One of the most common parts that uses VAR-processed alloys are turbine blades, which can be found in airline jet engines. The safety of a everyone on board depends on these parts not failing. Not only are imperfections dangerous, they are also hard to find, giving even more motivation to streamline and perfect the VAR process. VAR furnaces can be equipped with video cameras that monitor the melt through the annulus. This does not give quantitative information on the arc behavior, and is mainly used for side-arc detection. Side arcing is when the arcs are formed between the electrode and the crucible, instead of the ingot. This can result to dangerous scenarios where not only the part is compromised but also the furnace and safety of nearby operators. However, Woodside et al. recently developed arc position sensing technology using magnetic field measurements to determine arc locations. The technology uses magnetostatic simulations of furnaces with magnetic field sensors to locate arcs. The model used to run simulations is key to the system, and is used for individual furnaces as they range in geometry, and even location. Refinement and further analysis on the model could lead to a more accurate and refined arc position sensing technology, and therefore aiding the industry improve the process efficiency. The objectives of this research are to, first, recreate results from Woodside et al. [15]. Creating a model that matches published results confirms that the methodology employed here is valid. When parameters in the model are then changed, these results can be compared to analyze changes in accuracy. The analysis of how real world phenomena can alter model results is the second objective of the study.

The main goal of arc position sensing technology is to accurately determine arc location during the process, this information can be used to better understand how imperfections happen. In order to accomplish this, the solidification of the ingot is modeled, and numerical experiments are performed in the attempt to understand how arc location affects the final product. Looking even further into the future, if I can develop an accurate arc position sensing technology, and then deduce what arc motion results to either perfect ingots or imperfect ingots, it could be possible to control the arc using externally

applied magnetic fields to produce quality products consistently.

1.3 Thesis structure

This thesis is structured as follows. Chapter 1 gives an introduction of vacuum arc remelting at a broad level, and motivation is provided as to why these studies were performed. Chapter 2 describes a sensitivity study on arc position sensing technology developed by Woodside et al. This approach employed certain assumptions, and Chapter 2 both replicates past results and studies how changing some of these assumptions alters the accuracy of arc location predictions. Being able to locate arcs in real time would be extremely beneficial for the industry, but more research has to be done on how exactly arc behavior affects the ingot. Chapter 3 studies solidification of a VAR ingot. There have been multiple solidification studies specializing in VAR furnaces. However, how arcs affect the solidification has not been one of their main targets. In Chapter 3 I look into this variable of VAR. A computational fluid dynamics model simulates how arcs affect the liquid metal in the ingot and the resulting solidification. Chapter 4 ties the subjects together and draws overall conclusions and as outlines potential future work.

Chapter 2: Sensitivity analysis of an approach for detecting arc positions during vacuum arc remelting based on magnetic flux density measurements

2.1 Abstract

Vacuum arc remelting (VAR) is a melting process for the production of homogeneous ingots, achieved by applying a direct current to create electrical arcs between the input electrode and the resultant ingot. Arc behavior drives quality of the end product, but no methodology is currently used in VAR furnaces at large scale to track arcs in real time. An arc position sensing (APS) technology was recently developed as a methodology to predict arc locations using magnetic field values measured by sensors. This system couples finite element analysis of VAR furnace magnetostatics with direct magnetic field measurements to predict arc locations. However, the published APS approach did not consider the effect of various practical issues that could affect the magnetic field distribution and thus arc location predictions. In this paper, I studied how altering assumptions made in the finite element model affect arc location predictions. These include the vertical position of the sensor relative to the electrode-ingot gap, a varying electrode-ingot gap size, ingot shrinkage, and the use of multiple sensors rather than a single sensor. Among the parameters studied, only vertical distance between arc and sensor locations causes large sources of error, and should be considered further when applying an APS system. However, averaging the predicted locations from four evenly spaced sensors helps reduce this error to no more than 16 % for a sensor position varying from 0.508 m below and above the electrode-ingot gap height.

2.2 Introduction

Vacuum arc remelting, or VAR, is the metallurgical process of remelting metal ingots with the application of a direct current into the system, in a vacuum environment. The result is a high-quality metal ingot that exhibits increased homogeneity and decreased de-

fects. The high-quality metals produced by VAR are typically used for high-performance applications such as aerospace systems [17]. VAR is often used on Ni- and Ti-based alloys [10, 15, 16, 20].

Figure 2.1 depicts a VAR furnace cross section. The current applied to the system forms electrical arcs between the melted ingot and the input consumable electrode. Since no ingot exists at the start of the process, common practices include the addition of small metal pieces to the bottom of the crucible to form an arc. These arcs begin the melting process of the electrode, which then transfers mass to the bottom of the crucible due to gravity. This mass solidifies at the bottom of the ingot as the arcs and heat transfer take place at the electrode-ingot gap, which travels up the crucible as more mass is transferred from the electrode to the ingot. Arcs can simultaneously form in multiple positions; presently, operators can neither visualize nor control the formation of arcs. A water-cooled jacket prevents the copper crucible from melting. At the top of the melted ingot a liquid pool of the material exists. The characteristics of this melt pool have a large impact on final quality of the ingot [2, 16, 20].

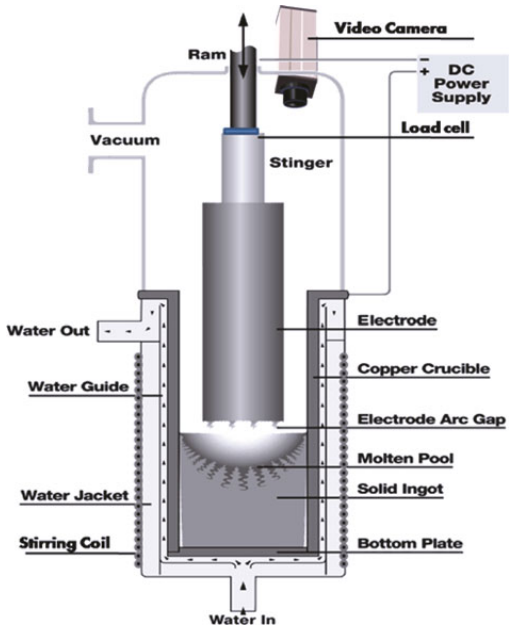

Figure 2.1: Cross section of VAR furnace. Image taken from Woodside et al. [15]

Arc behavior drives the remelting process and determines ingot quality, but arc positions are challenging to quantify due to the VAR system geometry and high-temperature environment. Currently, video cameras directed down the annular gap between the electrode and crucible give operators qualitative information of arc behavior, as well as side arc detection, however these systems cannot track instantaneous arc formation and motion. A robust arc detection and tracking system would give insight into the material properties of the final ingot. A common approach for detailed study of VAR furnaces is numerical modeling [2, 5, 10, 11, 13, 15, 16, 20]. The application of large currents through the system results in a strong magnetic field surrounding the furnace, on which several studies focused [9, 13, 15]. The arc position in the ingot-electrode gap is a key parameter that affects the magnetic field. Arcs concentrate the electrical current passing through the system and impact the distribution of the magnetic field.

Mir et al. [8] studied the thermal behavior of the consumable electrode using infrared cameras, focusing on heat transfer characteristics. However, their technique required alteration of a furnace and revealed little insight on arc behavior. Zhao et al. [20] used the two-dimensional finite element software ANSYS to study fluid dynamics in the molten pool. The model assumed that only buoyant forces act on the melt pool, the melt pool exhibits turbulent flow properties, chemical reactions are negligible, and material properties depend only on temperature. They did not consider the effects of arc location on the melt pool, but mentioned it as a source of interest. Gartling et al. [5] created a numerical model of the VAR process that delivered qualitatively accurate results. They emphasize one of the parameters that needed to be addressed are the characteristics of melt pool stirring due to electromagnetic, and therefore arc, characteristics. Reiter et al. [11] simulated heat transfer in VAR ingots during the melting process, where the coupling of an electromagnetic mathematical model was essential for accurate results. Pericleous et al. [10] developed a three-dimensional transient multi-scale model that incorporated a macro-level FEM-based computational fluid dynamics model coupled with a microscale solidification model to study VAR processes. They found that arc location and characteristics drive the occurrence of “freckles” and “white spots,” two key defects in the quality of VAR ingots [10]. Wang et al. [13] developed a two-dimensional axisymmetric model to study arc characteristics under different axial magnetic fields using the commercially available software Fluent. Their model focused on magnetohydrodynamics and plasma behavior in the electrode-ingot gap, assuming that plasma consisted of

only electrons and ions and its flow can be described with a hydrodynamic approximation. They concluded that the effect of current density distribution, arc distribution, was significant for VAR because it directly correlates to the heat flux density at the anode. Woodside et al. [14, 15] used the multiphysics finite-element modeling (FEM) software COMSOL to simulate the magnetostatics of a VAR furnace. They assumed an axisymmetric furnace, homogeneous material properties, and a single non-diffuse arc in a three-dimensional model. Model results were used to develop a relationship between measured magnetic field readings at a notional Hall sensor position and arc locations [15]. Nair et al. [9] used the FEM software Opera3d to study the use of magnetic source tomography to understand arc behavior in VAR systems. They modeled electrostatics while assuming homogeneous material properties, and included both single and double non-diffuse arcs. Nair et al. concluded that arc locations can be predicted based on measurements of magnetic flux density outside the furnace with sufficient accuracy under the right circumstances. According to literature, arc locations and characteristics directly affect ingot characteristics. [5, 9–11, 13, 15, 20] Various studies showed that arc locations can be predicted accurately using magnetic flux density measurements around VAR furnaces combined with accurate numerical models. [9, 15] However, these methodologies made assumptions and simplifications that should be validated further to encourage their application in industry.

The purpose of this study is to model the magnetostatics of the VAR process in different scenarios, while evaluating the impact of previously made assumptions, to determine the potential errors of arc locations predicted by the Arc Position Sensing (APS) system of Woodside and King [14]. Understanding the behavior of the APS technology due to changing parameters could lead to further validation or improvement [9, 15]. I used a multiphysics FEM simulation software to study the system. First, in Section 2.3 I describe the methodology and approach used to establish a working model of the system, and discuss the methodology of the arc location prediction equations. Next, in Section 2.4, I inspect several factors that may impact the accuracy of arc location predictions, including the vertical distance between the sensor and arc, the size of the electrode-ingot gap, the effects of ingot shrinkage, and the use of multiple sensors. Finally, in Section 2.5 I summarize my results into primary conclusions, and make some recommendations of best practices for using—and further developing—the APS technology.

2.3 Methodology

In this section, I describe my approach to modeling the VAR furnace and predicting arc locations based on model results. The multiphysics FEM software COMSOL Multiphysics [4] to simulate a simplified VAR furnace, with arcs located in different locations in the electrode-ingot gap. Our model only considered magnetostatics, based on the steady-state Ampere's Law and current conservation equation:

$$\mathbf{J} = \nabla \times (\mu_0^{-1}\mu_r^{-1}\mathbf{B}) - \sigma\mathbf{v} \times \mathbf{B} \tag{2.1}$$

$$\mathbf{B} = \nabla \times \mathbf{A} \tag{2.2}$$

$$\nabla \cdot \mathbf{J} = 0 \tag{2.3}$$

where $\mathbf{J}$ is the current vector, μ_0 is the permeability of a vacuum, μ_r is the relative permeability of the material, $\mathbf{B}$ is the magnetic flux density vector, σ is the electrical conductivity, $\mathbf{v}$ is the particle velocity, and $\mathbf{A}$ is the magnetic vector potential.

Table 2.1: Geometric specifications of modeled VAR furnace

Component	Radius (m)	Height (m)
Electrode	0.381	1.000
Ingot	0.432	1.057
Crucible (outer)	0.472	4.000
Crucible (inner)	0.432	4.000
Furnace shell (outer)	0.640	4.000
Furnace shell (inner)	0.472	4.000
Arc	0.010	0.0254

I modeled a simplified axisymmetric VAR furnace, based on the geometry of Woodside et al. [15]. Table 2.1 lists the geometric specifications, and Fig. 2.2 shows the geometry of the VAR furnace studied. The electrode and ingot were both assumed to be titanium, with an electrical conductivity of $7.407 \times 10^5\,\mathrm{S/m}$ and relative permeability of 7.9585×10^{-7}. The surrounding crucible was selected as copper (electrical conductivity of $5.998 \times 10^7\,\mathrm{S/m}$ and relative permeability of near 1), and the outer shell as steel (electrical conductivity of $4.032 \times 10^6\,\mathrm{S/m}$, and relative permeability of near 1). The annular space between the electrode and crucible and the electrode-ingot gap were modeled as

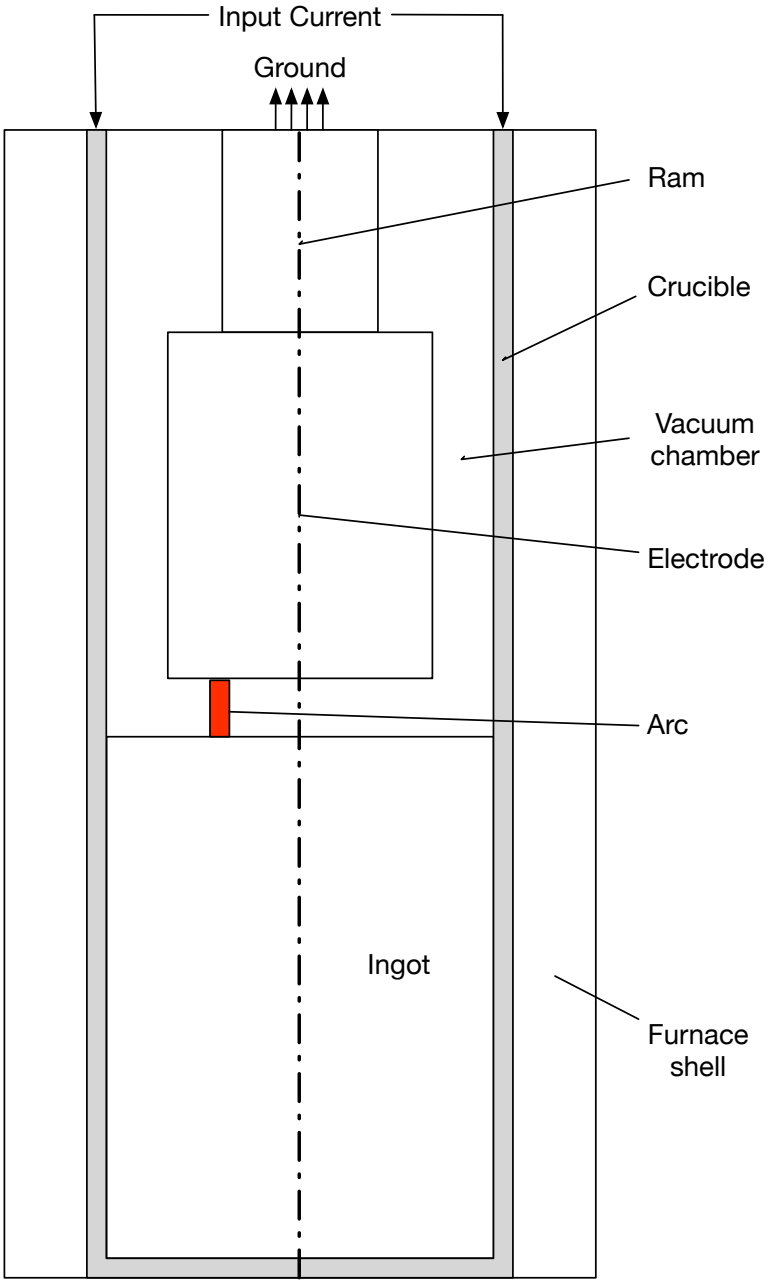

Figure 2.2: Diagram of the geometry employed in the model (not to scale)

near-vacuums, with an electrical conductivity of essentially zero (1×10^{-15} S/m), and relative permeability of exactly 1.0. A small cylinder connecting the ingot and electrode represented the arc, with all current forced through that small location; the arc was assigned an electrical conductivity 20 orders of magnitude larger than its surroundings. The size of the cylinder has minimal effects on the magnetostatics of the scenario if its position and current remain constant. [9]. Another simplification applied to the model is the assumption that principles of superposition can be used in order to take into account the effects of multiple arcs. [15]. The application of superposition was utilized by both Woodside et al. as well as Nair and Ward [9, 15]. The top of the copper crucible was assigned a current source of 35,000 A, and the system was grounded at the ram that feeds the electrode. Domain boundary conditions were set to mimic an infinite domain. The entire domain used a mesh consisting of free tetrahedral cells, that was automatically determined by COMSOL. I assigned the mesh size near the electrode-ingot gap as "fine" settings, with a minimum element size of 0.0016 m. The rest of the furnace geometry was set to "medium" settings, with a minimum element size of 0.08 m. The outer boundary was set to "coarse" mesh settings, with a minimum element size of 0.224 m. Mesh settings resulted in a total element count of approximately 170,000. Further refining the grid changed solutions to within 5 % of the results published here, so I selected the aforementioned settings as a tradeoff between acceptable accuracy and time-to-solution.

Next, I simulated sensor readings from one location. A point was chosen in the three-dimensional space of the domain to represent the sensor location; a physical sensor itself was not modeled, as its presence should not affect the magnetic field distribution. Parametric sweeps were performed of the arc location to calculate flux density changes at the sensor location. (Swept parameters in COMSOL include r_0 and θ_0, where r_0 is the radial position of the arc from the center of the furnace and θ_0 is the angular position of the arc with respect to the x-axis.) Figure 2.3 shows the magnetic flux density (T) as a function of arc position for a sensor located at (0 m,—0.64 m).

Arc position predictions can now be examined. As determined by Woodside et al. [15] arc position determination can be achieved through the application of the Biot–Savart law. The Biot–Savart law with a magnetostatic derivation of the Maxwell–Ampere law, using the relation between superimposed line sources of current, and magnetic flux density

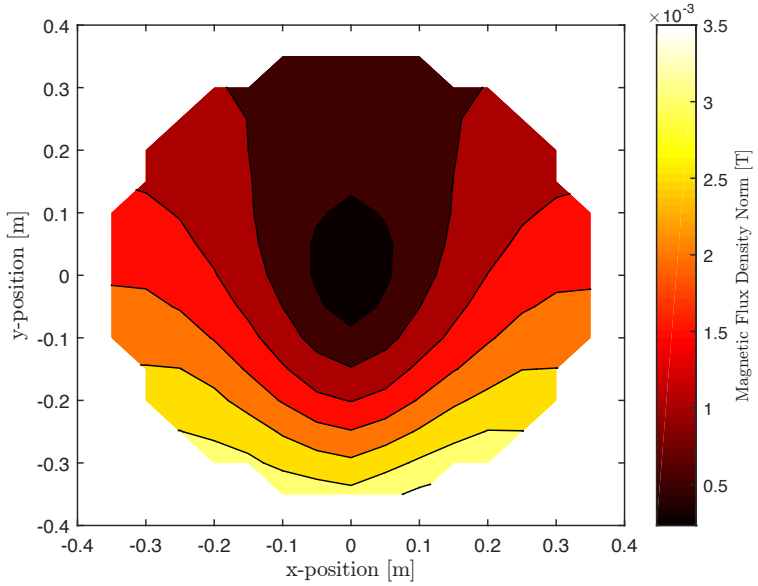

Figure 2.3: Magnetic flux density norm with respect to arc location in Cartesian coordinates

vector $\mathbf{B}$ at a location $\mathbf{r}$ is given by

$$\mathbf{B}(\mathbf{r}) = \frac{\mu_0}{4\pi} I \int \frac{d\mathbf{I}' \times \hat{\mathbf{r}}}{\|\mathbf{r}\|^2} \,, \tag{2.4}$$

where $d\mathbf{I}'$ is an element of the length along the total current, $\mathbf{r}$ is the vector from the source to the point, and $\hat{\mathbf{r}}$ is the unit vector of $\mathbf{r}$. This equation can be used to find the components of the magnetic field:

$$\mathbf{B}_t = m_t I \left(\sum \frac{f_i \sin\theta_i}{d_i} - \frac{1}{r_s} \right) \,, \text{ and} \tag{2.5}$$

$$\mathbf{B}_r = m_r I \left(\sum \frac{-f_i \cos\theta_i}{d_i} \right) \,. \tag{2.6}$$

where $\mathbf{B}_t$ and $\mathbf{B}_r$ are the tangential and radial components of the magnetic flux density, m_t is the tangential furnace coefficient, m_r is the radial furnace coefficient, I is the line current, θ_0 is the input angle in the model of an arc, from the center of the furnace, d_0 is

the input radius of an arc, from the center of the furnace, θ_i is the angle from the sensor to the arc location, d_i is the length from the sensor to the arc location, r_s is the distance from the sensor to the center of the furnace, and f_i is the fraction of the total current associated with the arc.

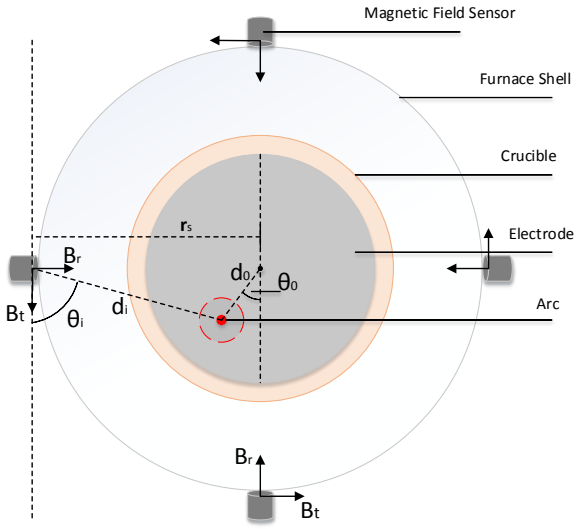

Figure 2.4: Overhead cross-sectional diagram of a VAR furnace, shown with four two-axis magnetic field sensors and the geometry of the variables for one sensor

Figure 2.4 shows a top-down cross-section of the VAR furnace modeled, including sensor locations. The furnace coefficients m_t and m_r depend on the geometry and configuration of individual furnaces [15]. The input angle for the COMSOL model and the angle θ are different measurements. Using the Biot–Savart equations, a nonlinear regression was used to determine the unknown furnace coefficients m_t and m_r. Once these were determined, the single-line current versions of the Biot–Savart equations were solved for d_i and θ_i (according to Fig. 2.4) with input or measured magnetic flux density components. A vector reference frame rotation and translation is done to transform the magnetic field values from the reference of the center of the furnace to each sensor

location. The equations take the form

$$d_i = \frac{I m_r m_t}{\sqrt{\frac{I^2 m_r^2 m_t^2}{r_s^2} + \frac{2IB_t m_t m_r^2}{r_s} + B_r^2 m_t^2 + B_t^2 m_r^2}} \text{ , and} \tag{2.7}$$

$$\theta_i = \cos^{-1}\left(\frac{-B_r d_i}{m_r I}\right) . \tag{2.8}$$

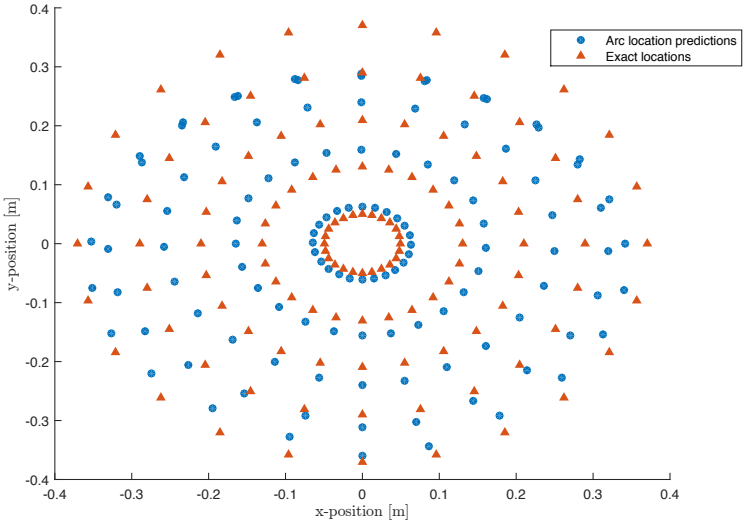

Figure 2.5: Predicted arc locations compared to exact locations (calculated using furnace coefficients $m_r = 8.15 \times 10^{-8}\,\mathrm{N/A^2}$, $m_t = 4.98 \times 10^{-8}\,\mathrm{N/A^2}$)

These equations represent the basis of the APS technology [15]; using a given geometry and FEM-based furnace coefficients, the arc can be located using measurements of magnetic flux density and the current through the system. Performing a parametric sweep of arc locations in the model results in magnetic flux density components at the sensor location. This array of values is equivalent to experimentally measured sensor magnetic flux density values. Figure 2.5 shows the predicted arc locations in contrast to the exact locations. Table 2.2 compares the furnace coefficients found here with those of Woodside et al. [15]; my implementation predicts arc locations within five percent of the published values. This discrepancy likely resulted from slight differences in geometry or solver setup (the model was developed based on published descriptions), differing

COMSOL versions, or a different selection of input arc locations to calculate the furnace coefficients.

Table 2.2: Comparison of furnace coefficients from Woodside et al. [15] with those determined here

	m_r (N/A^2)	m_t (N/A^2)
FEM results	8.15×10^{-8}	4.98×10^{-8}
Woodside et al.	9×10^{-8}	4.9×10^{-8}

The remaining sections of the paper describe the performance of the arc position sensing approach as various model parameters are varied or assumptions are relaxed. This performance is described in terms of percent error in the predicted arc locations with respect to the known arc locations, normalized by the ingot radius (0.432 m). The error is determined as the difference between two position vectors, the predicted and exact locations of the arc.

$$error = \frac{\sqrt{(x-\hat{x})^2 + (y-\hat{y})^2}}{radius_{ingot}} * 100 \tag{2.9}$$

where x, y are the exact positions and $\hat{x}$, $\hat{y}$ are the predicted positions.

2.4 Results and discussion

In this section, I describe the results of my studies on the impact of various factors on the accuracy of arc location predictions. I considered the effects on arc location predictions of vertical sensor position (i.e., relative vertical distance between the sensor and arc), electrode-ingot gap size, ingot shrinkage, and using the average of predictions from multiple sensors. All error calculations were based on the difference between the known position specified in the COMSOL model and the location predicted using Eqs. (2.7) and (2.8).

2.4.1 Effect of vertical sensor position

The original APS studies of Woodside et al. [14, 15] considered a single sensor located in the plane of the electrode-ingot gap, where theoretically the most accurate results would be achieved due to the line-current source assumption. In reality, due to the continuous movement of the electrode and growth of the ingot, the sensor would be in that plane only for a small amount of time relative to the the entire process. In addition, ingots used for industrial VAR applications can be several meters in length amplifying any error caused by deviation from the electrode-ingot gap. A solution to this problem is the application of multiple rings of sensor installed in intervals that lie within acceptable error. I therefore want to quantify the potential error induced by a vertical separation between sensor and arc, in order to decide how frequently or far apart sensors should be placed along a furnace. To determine the error of vertical distance between the arc and sensor, I varied the vertical sensor position away from the plane of the gap in multiples of the electrode-ingot gap height: ±0, 1, 2, 3, 5, 7, 10, 15, and 20.

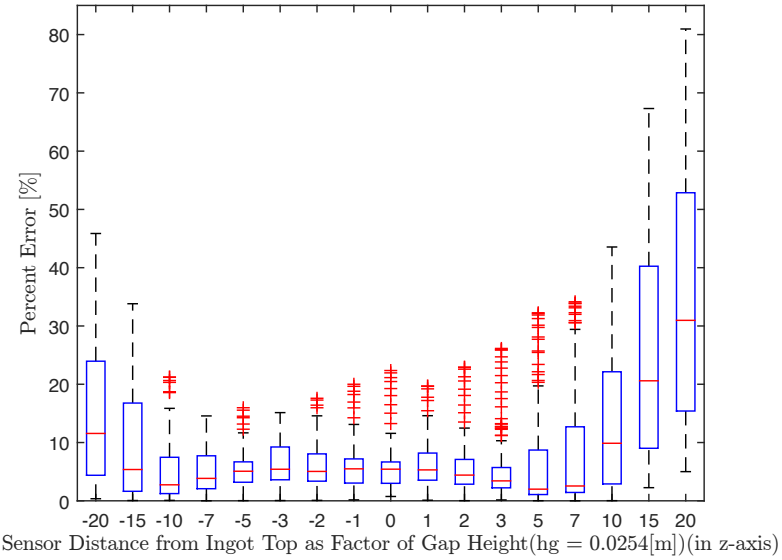

Figure 2.6: Statistical error distribution of predicted arc locations with respect to vertical sensor position using constant furnace coefficients

Figure 2.6 shows a box-and-whisker statistical distribution of the percent error in

predicted arc position with respect to vertical sensor position using a single sensor; clearly, the error increases both as the sensor moves above and below the gap. The red line inside the rectangles represents the median, the blue boxes span the 25th and 75th percentiles of the data, and the black whiskers span the maximum and minimum values not defined as outliers. Outliers—defined as values greater than three times the standard deviation—are represented by red plus-sign markers. Interestingly, the trend in increasing error is asymmetric, with error increasing more rapidly for sensor locations above the gap. The asymmetry observed in error is most likely caused by the asymmetry of the current loop in the system. The reasons for the error being lower for sensors below the electrode-ingot gap is not clear.

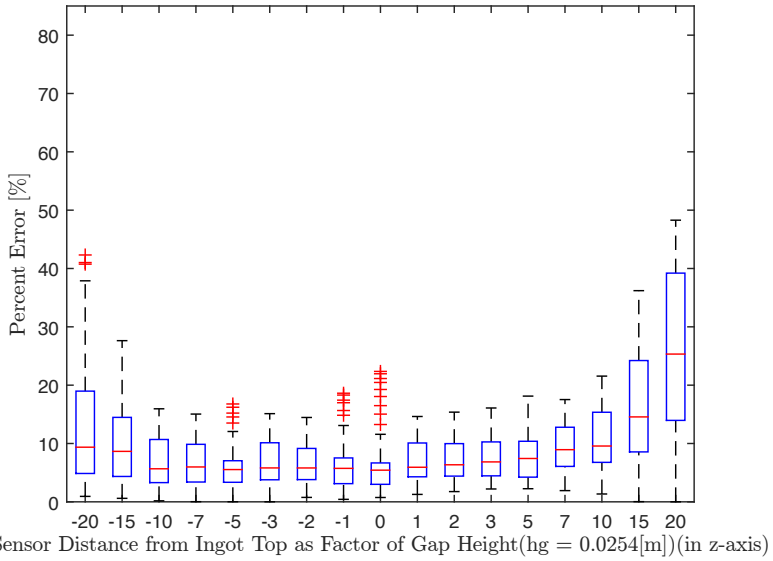

Figure 2.7: Error distribution of predicted arc locations with respect to vertical sensor position using adaptive furnace coefficients

For the results shown in Fig. 2.6, arc locations were predicted assuming constant furnace coefficients determined using data for a sensor placed at the plane of the electrode-ingot gap. The coefficients can also be recalculated for each sensor position, and investigated whether this practice improves results. This procedure is identical to that of the normal coefficient calculation, but uses magnetic flux density measurements at the vari-

ous vertical sensor locations (rather than in the plane of the gap). Figure 2.7 shows the distribution of error in predicted arc locations using furnace coefficients recalculated for each sensor location. The varying furnace coefficients aided in suppressing outliers, and reducing maximum error. For the sensor position of $20\times$ h_g, using varying coefficients reduced maximum error by more than 30 %, and decreased median error by approximately 5 %. Median error shows a slight increase for all vertical sensor positions; however, using varying furnace coefficients reduced the overall distribution of error. The application of varying furnace coefficients decreased maximum error by 9.27 % on average for all sensor locations, compared to using constant coefficients. Looking at four points in more detail, for a sensor located $5\times$ above and below the gap, median error for variable coefficients increased by 5.43 % and decreased by 0.46 % respectively, compared to their constant coefficient counterparts. For a sensor located $10\times$ above and below the gap, median error decreased by 0.31 % and increased by 2.92 %, respectively. In real world systems the true vertical position of the electrode-ingot gap is unknown, however reasonable estimates can be made using data from the melt such as weight and size of the ingot, time, and ram position. Including this step in the algorithm could result in higher accuracy as shown in the results, however it would require real-world testing and experimentation to confirm.

While percent error at each location offers some information about measurement accuracy, examining the actual predicted locations and how they change can give insight on trends. Figure 2.8 shows arc location predictions as the sensor location moves from the electrode-ingot gap plane upwards along the furnace wall, for vertical sensor locations of 0, 0.0762, 0.254, and 0.508 m (or 0, 3, 10, and 20 h_g). As the sensor position moves away from the electrode-ingot gap, the arc location predictions cluster together near the center of the furnace. I hypothesize that this results from the current density concentrating inwards inside the electrode as it traverses through the electrode and into the smaller-radius ram. The equations used to locate arc positions are two dimensional, using tangential and radial magnetic flux values in the plane of the sensor's vertical position. The magnetic flux values measured by sensors positioned away from the electrode-ingot gap plane are small; for example, a sensor positioned at the electrode-ingot gap plane, a maximum of 3.3×10^{-3} T in the radial direction and 3.5×10^{-3} T in the tangential direction are observed. On the other hand, a sensor located 0.5 m above the electrode-ingot gap measures a maximum of 2.5×10^{-4} T in the radial direction and 7.5×10^{-4} T in the tangential direction. In Eqs. 2.7 and 2.8 used to calculate position, magnetic flux

components appear in the denominator—so the order-of-magnitude smaller values at the higher sensor location result in predicted locations further away. However, Fig. 2.8 shows that the location predictions shift further away and also cluster around the center of the furnace. This supports the hypothesis that the electrical current funnels as it traverses the electrode, and the magnetic flux density values being measured at sensor locations away from the gap is the current density in the electrode for that plane. This clustering behavior would impact results by indicating the presence of arcs near the center of the furnace, when they might actually occur near the edges of the electrode and ingot.

2.4.2 Effect of gap size

All previous calculations assumed a constant electrode-ingot gap. In theory, the gap size should remain approximately constant as the ram raises the electrode based on its melting and solidification rate; in reality, the gap size is constantly changing slightly throughout this process. This variation could introduce non-negligible errors into the predictions of arc locations, and therefore I studied the effect of gap size on the accuracy of arc location predictions. Previous studies set the gap height to a constant 0.0254 m [14, 15]; here, I varied the height between 0.5–2.5 times the baseline value, or specifically 0.0127, 0.0254, 0.0381, and 0.0635 m. Gap sizes considered in the literature include 0.01 m [2, 9] for smaller radius ingots/electrodes, although Zanner studied the effect of gap sizes ranging 0.006–0.05 m [18] on melt rate.

Figure 2.9 shows arc location predictions with varying gap height for a single sensor location. The error in arc location prediction exhibits little sensitivity to gap height; between the smallest and largest gap heights, the median error differs by less than 1.5 % and the maximum error by less than 5 %.

2.4.3 Effect of ingot shrinkage

The physical characteristics of the ingot differ drastically from top to bottom during the melting process. At the top, a molten pool of liquid metal circulates on top of the soft, hot metal solidifying near the sides and bottom. As the VAR process continues and the ingot grows, the metal cools and contracts. This causes the metal to shrink and pull away from the crucible, reducing the electrical contact surface area with the

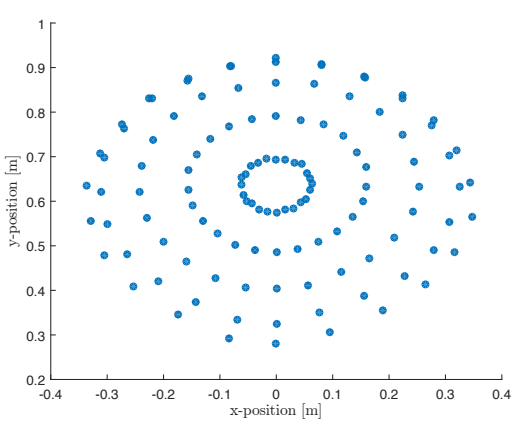

(a) Arc location prediction with a sensor at the electrode-ingot gap

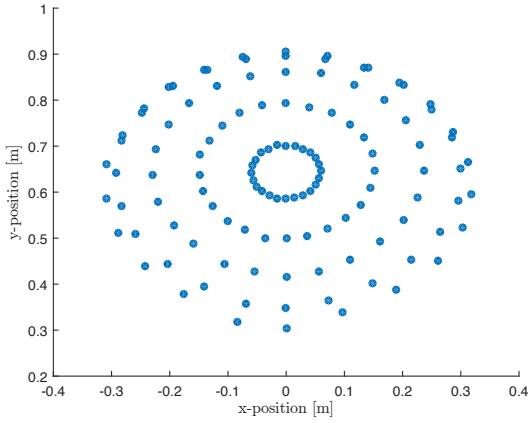

(b) Arc location prediction with a sensor 0.0762 m above the electrode-ingot gap

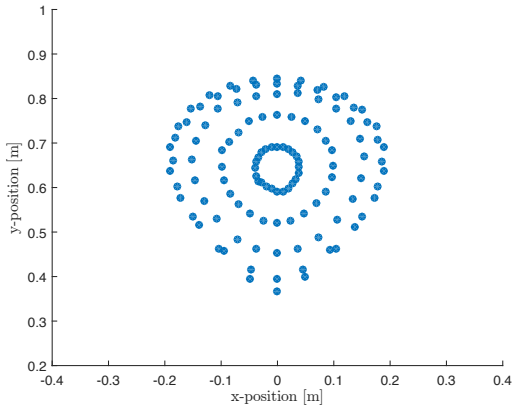

(c) Arc location prediction with a sensor 0.254 m above the electrode-ingot gap

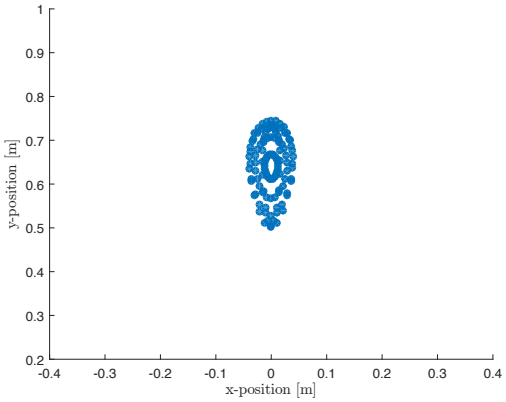

(d) Arc location prediction with a sensor 0.508 m above the electrode-ingot gap

Figure 2.8: Arc location prediction trends for varying, single sensor position in the positive z direction with the origin at the sensor location (0,0.64 m) using constant furnace coefficients

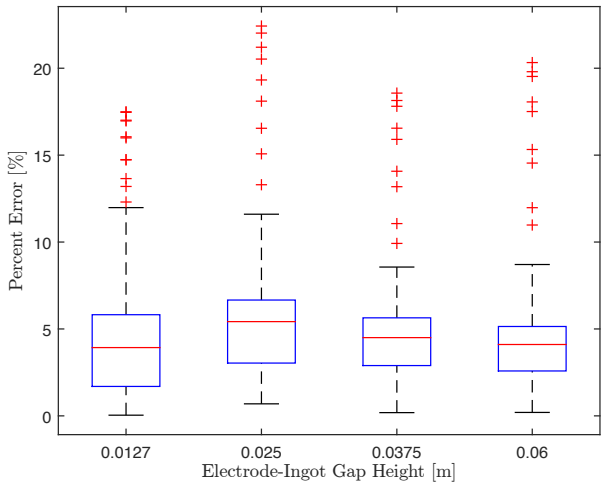

Figure 2.9: Arc location predictions with varying gap height for a single sensor location

crucible; this behavior is known as ingot shrinkage. The section of the material that remains in contact with the crucible wall is called the contact zone. Since shrinkage changes the surface area of the ingot that contacts the crucible wall—and thus the area where electrical current passes—it could alter the current path and thus the magnetic field distribution, potentially affecting predictions of arc location. I studied the effects of shrinkage by applying grounded boundary conditions to the contact zone and electrical insulation to the shrinkage gap zone, following the approach of Pericleous et al. [10]. I varied the size of the contact zone from the full length of the ingot to 0.032 m, ranging from zero shrinkage to a contact zone 3 % of the ingot height.

Figure 2.10 shows the error distribution for predicted arc locations with increasing shrinkage, corresponding to decreasing contact zone height. While error increases slightly as the contact zone shrinks, in general shrinkage causes an median error increase of less than 2 % in predicted arc locations, corresponding to a similar change in magnetic flux density. However, the higher current density resulting from smaller contact zones could affect the z component of magnetic flux density more significantly—although this component does not play a role in the current APS approach based on horizontal (i.e., x and y) components.

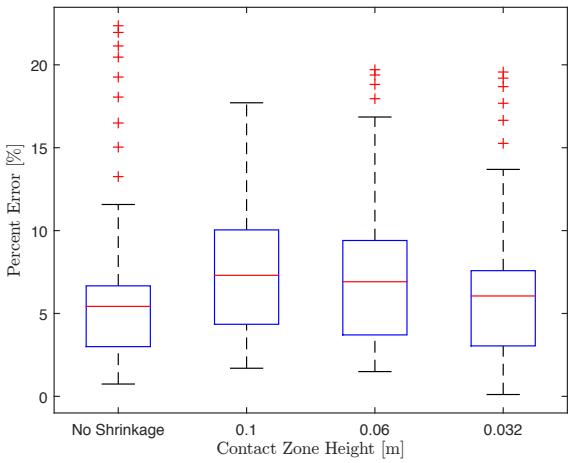

Figure 2.10: Error in predicted arc locations with varying contact zone height, mimicking ingot shrinkage

2.4.4 Effect of using multiple sensors

Thus far, I only used magnetic field measurements at one sensor location for calculations to determine arc locations. Both my results and those from Woodside et al. [14, 15] show that the error increases as the arc moves away from the sensor. Therefore, for an axisymmetric system, I hypothesize that the results from multiple sensors can be averaged to improve the accuracy of the overall prediction. To test this, I averaged predicted arc locations from 2–16 evenly spaced sensors around the furnace.

First, I examined the trends in arc location prediction for two separate sensors located at opposite sides of the furnace; Figure 2.11 shows these (separate) predicted arc locations, compared with the exact locations. Although the sensors predict similar locations for arcs located near the center of the furnace, near the perimeters the predicted locations exhibit a bias towards the closer sensor. Figure 2.12 compares exact arc locations with predictions based on the average location from four evenly spaced sensors. The averaging resulted in an even spacial distribution of the arc positions; as Figure 2.13 shows, the error predicted locations is also evenly distributed compared with that from a single sensor. This information is useful because it can be used to develop correction algorithms to predict arc locations more accurately. Based on these results, more sensors might aid in

smoothing the error further; however, evenly distributed results do not guarantee more accurate results—in fact, outliers could bias the predictions. Figure 2.14 shows the error distribution in predicted arc locations achieved by averaging calculations using 1, 2, 4, 8, and 16 evenly distributed sensors. The error distribution contracts with the addition of sensors, but the predictions do not improve with more than four sensors.

Now I can analyze whether using four sensor averaging of arc location predictions aid in the reduction of error for a varying sensor height. In Section 2.4.1 I calculated how error distribution was affected by the relative vertical position of a single sensor with respect to the electrode-ingot gap. Now, I apply the same methodology while using arc location predictions determined with four-sensor averaging. The results are shown in Figure 2.15. The total error distribution is smaller than the single-sensor results from Section 2.4.1 with a maximum error of less than 16 % at the highest and lowest positions. Using four sensors also suppresses the outliers. These results were calculated using varying furnace coefficients; the coefficients were recalculated at every vertical position.

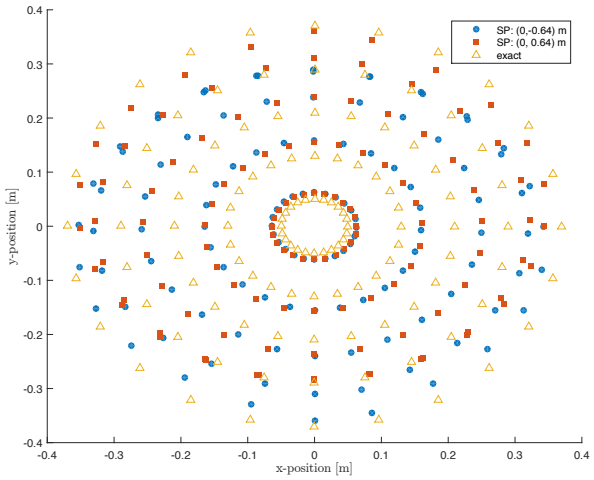

Figure 2.11: Arc location predictions for two sensors position on opposite sides of the furnace: (0 m, −0.64 m) and (0 m, 0.64 m)

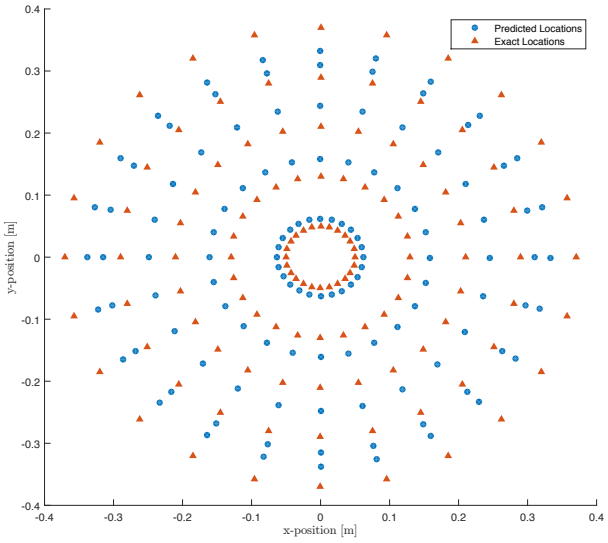

Figure 2.12: Arc location predictions using four sensors around the furnace; these locations are the average of the locations predicted by each of the four sensors

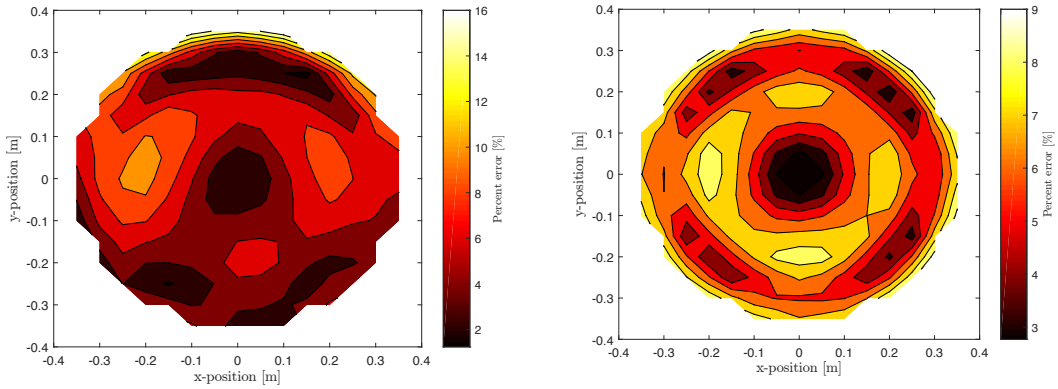

(a) Percent error of arc location predictions using one sensor

(b) Percent error of arc location predictions using four sensor averaging

Figure 2.13: Comparison of error distribution and magnitude from using one sensor versus four sensor averages; error is based on difference between predicted and exact values

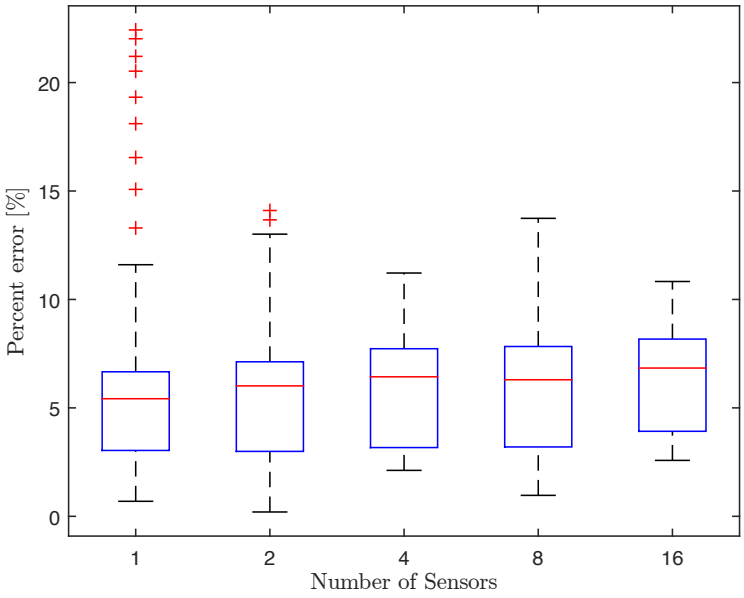

Figure 2.14: Percent error statistical distribution for 1, 2, 4, 8, and 16 sensors

2.5 Conclusions

The magnetostatic characteristics of a simplified vacuum arc remelting furnace where studied using the finite element method, in order to determine the effects of various physical phenomena on the resulting magnetic field. This was done to validate a system for predicting the locations of electrical arcs that form in the electrode-ingot gap in these furnaces. Arc distribution throughout the remelting process plays a strong role in the material properties of the produced ingot, so real-time tracking of arc locations can provide a priori indications of ingot quality.

First, I reproduced the prior results of Woodside et al. [15] for predicting arc locations; I matched arc location predictions within 3.5 % of their results. This minor discrepancy likely resulted from slight differences in model setup, solver version, or selection of input arc locations to calculate the furnace coefficients. I then studied the effects of changing certain parameters or eliminating previously made assumptions to validate this overall approach for the arc position sensing technology. Based on my simulations, I drew the following conclusions:

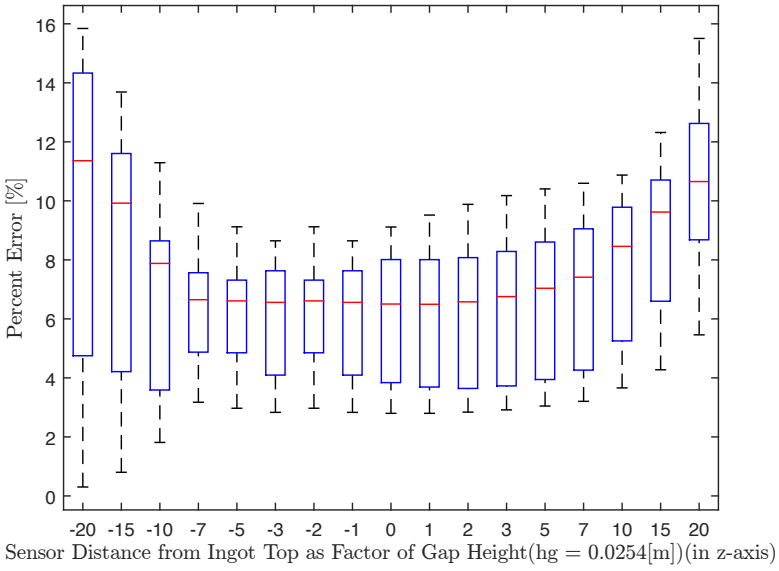

Figure 2.15: Error distribution of predicted arc locations with respect to vertical sensor position using the average results from four sensors

1. Error in predicted arc locations increases substantially as the sensor moves vertically from the electrode-ingot gap; for distances of 0.508 m above and below the plane of the gap, the maximum error reached around 40 % for constant furnace coefficients and 25 % for adaptive furnace coefficients. Furthermore, as the sensor moves away from the gap, the magnetic flux density decreases and results in clustering of predicted locations near the center of the domain.

2. Gap height variations do not significantly affect predictions in arc location: varying the gap height from 0.0128 m to 0.063 m resulted in the median error changing by 0.55 % and the maximum error by 1.65 %.

3. Ingot shrinkage does not affect predictions in arc location; varying the ingot contact zone from the entire length down to 0.032 m kept the maximum error around 10 %, and did not change the median error of around 2 percent.

4. Averaging the measurements of four evenly spaced sensors around the furnace reduces prediction error distribution by 12.64 % compared to a single sensor ; there is

little to no improvement on location predictions with the implementation of more than four sensors. The total error distribution reduces by 0.85 % comparing the implementation of four sensors against sixteen. The application of four sensor averaging aids in the suppression of error when taking into account vertical sensor position.

Overall, out of the parameters and assumptions I studied, I conclude that gap height variation and ingot shrinkage will not affect arc location predictions. However, increasing vertical distance between the sensor and arc will lead to significant errors in location prediction, and should be considered for further development of the arc position sensing technology.

Chapter 3: Effects of arc location on melt pool characteristics and solidification using finite volume methods

3.1 Abstract

Vacuum arc remelting (VAR) is a melting process of metal alloys for the production of homogeneous ingots, achieved by applying a direct current to create electrical arcs between the input electrode and the resultant ingot. These arcs melt the input material, or electrode, through Joule heating. Arc characteristics are key to the the final ingot's quality, how the liquid metal behaves as it solidifies can indicate characteristics that lead to imperfections, or that lead to reassurance of a good melt. Modeling the melt pool and its solidification is of interest due to the difficulty and cost of measurement and experimentation, and studying the effects of arc position on the melt pool and solidification is the main objective of the model. In this work the first building block towards towards a solidification model is presented. ANSYS Fluent 17.2 was used to model the fluid mechanics and heat transfer of the problem through the control volume approach. The model was simplified through the neglect of magnetohydrodynamics and studying a steady-state scenario. A uranium-niobium metal alloy was modeled. Results show that an arc located near the edge of the ingot, leads to a shallower solidification angle compared to a centered arc. The model exhibited velocity magnitude values within literature bounds where the melt pool velocities reach magnitudes of the order 10^{-2} m/s compared to the "pull" velocities in magnitude of 10^{-5} m/s. The melt pool will have its maximum velocity in the top and bottom portions of the circulating flow while the arc is centered, and will have its maximum velocity at the crucible interface when the arc is positioned at the edge of the ingot. Overall velocities increase when the arc is off-centered.

3.2 Introduction

Vacuum arc remelting (VAR) is the process of improving material properties of exotic metals through the application of high currents in a vacuum environment. The current

introduces high heat transfer through Joule heating that melts the input specimen, or electrode, and transfers material via gravity to a crucible. The crucible is surrounded by a water cooling system that expedites the solidification process. Figure 3.1 shows a diagram of a vacuum arc remelting furnace.

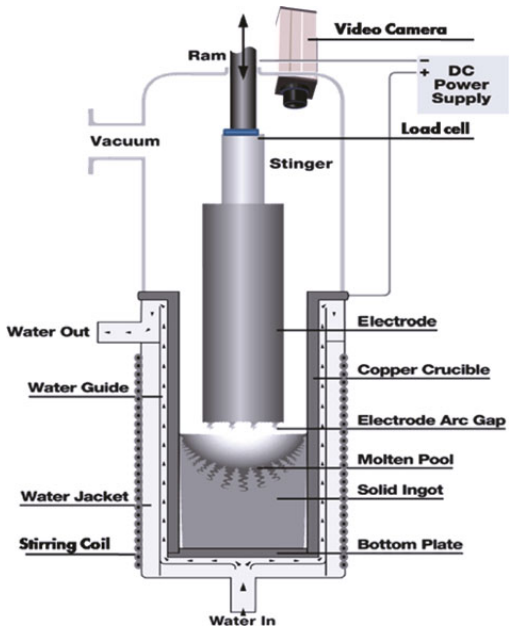

Figure 3.1: Cross section of VAR furnace. Image taken from Woodside et al. [15]

Electrical arcs form between the electrode and the resultant ingot; these arcs drive the whole process. They are the main source of melting and mass transfer of the electrode. Arc behavior is directly related to the quality of the final product [15]. One of the main benefits of VAR-treated metals is the increased homogeneity, both physically and chemically. Arc patterns distributed unevenly throughout the melt result in less homogenous ingots. Therefore, the electrical arcs in the VAR process are a crucial variable of interest for this industry. Currently there is no widespread technology used for real-time tracking of arcs; however, studies have shown that arc tracking is possible using simulation and sensors to measure the magnetic field around furnaces [9, 15]. The products of VAR are used in extreme environments such as aerospace and marine applications, so even single imperfections could result in catastrophic consequences. Having the ability to model and

study the solidification of the melt pool and mushy zone are critical towards this technology's progression [3]. The melt pool is the molten metal that exists at the top of the resultant ingot, while the mushy zone is is the layer of material in between the melt pool and the fully solidified ingot.

Beaman et al. [2] used spectral methods with an axisymmetric model to simulate the pool depth and characteristics for the goal to control and measure var melt pools in real time. They reiterate that ingot solidification is a vital part of the process that affects structural properties of the ingot, and is not controlled by in industry practice. Their system gives operators process control over the melt pool using a high-fidelity model run in parallel with the furnace [2]. Although their model succeeded in many ways, it felt short in accuracy. In particular, they identified the two-dimensianal axisymmetric model as a key parameter to improve results.. Kelker et al. [7] developed a computational model for the prediction of VAR performance using the control volume approach of Patankar. Their model includes the electromagnetics, turbulent flow in the pool, heat transfer, and macrosegregation for the duration of the entire process. They dived into effects of including magnetic stirring, but did not model what occurs when the arc is not centered. Pericleous et al. [10] developed one of the most thorough models in the literature, creating a three-dimensional full melt (transient) model that includes the effects of arc position. They were able to link the macroscale CFD model to the microscale solidification models. They focused on two specific defects: "freckles" and "white spots". Taking lessons learned from Pericleous et al [10] , I can create a model to inspect other sources of interest in industry such as arc effects on ingot solidification angle. Gartling et al. [5] developed a mathematical model for the transport phenomena and fluid flow in the ingot melt. They produced a model based on a two-dimensional axisymmetric finite element analysis (FEA), with a control volume that traverses as the ingot grows to create a "quasi-steady" solution of the melt. They incorporated the electromagnetism effects of the process, specifically how Lorentz forces affect the melt pool. However, they did not take into account arc position, which could be a critical part of how the liquid metal flow interacts and solidifies. Other numerical studies exist that follow along the same lines as those mentioned or describe defects in more material science detail. [11, 12, 16, 19].

The implementation of arc position as a parameter of interest forces the problem to move from an axisymmetric scenario. Ideally a three-dimensional model is strived for, but a good first step is a two-dimmensional non-axisymmetric model, where I can vary

the arc position from centered to off-centered. For now, this model will also neglect Lorentz force-induced motion of the liquid metal pool. In Section 3.3 I will outline the methodology, governing equations, and boundary conditions used to create a model that attempts to meet my goals. Section 3.4 will highlight and discuss results, before concluding statements are made in Section 3.5.

3.3 Methodology

The problem needs to be solved out for fluid flow and heat transfer. The finite volume software ANSYS Fluent v17.2 [1] was used to solve the governing equations. The finite volume method was selected because it offers multiple advantages for computational fluid dynamics, mainly how conservation is forced at cell walls and how pressure is coupled using multi-grid solvers. ANSYS Fluent can be used inside the software ANSYS Workbench, where different solvers can be combined to solve complex multi-physics problems. The software is written in C, and offers true dynamic memory allocation, efficient data structures, and flexible solver control [6]. Fluent uses ANSYS meshing software for mesh generation, which supports the creation of 2D triangular and quadrilateral, as well as 3D tetrahedral, hexahedral, pyramid, wedge, polyhedral, and mixed/hybrid meshes [6].

Instead of solving a rather large transient problem involving mass transfer at the inlet (in which there is zero mass at initial time) and the growth of the ingot, the scenario can be simplified to inspect the melt pool. The problem can be treated as "pseudo" steady-state if the reference frame moves at the rate equal to the melt rate, and only the top of the ingot is studied. This approach was used by Gartling et al. [5], and I will follow a similar approach here. For the numerical experiments here, the equations were solved using their transient forms until a steady state was achieved. Then, the arc is moved to the position desired for 5 seconds. After the simulation runs for 5 physical seconds, data is collected.

3.3.1 Governing equations

3.3.1.1 Continuity and momentum

The flow of the liquid metal portion of the ingot is described by the continuity equation, incompressible Navier–Stokes equations, and energy equation. The general form of the continuity equations is

$$\frac{\partial \rho}{\partial t} + \nabla \cdot (\rho \mathbf{v}) = 0, \tag{3.1}$$

where ρ is the fluid density,and $\mathbf{v}$ is the velocity vector. The continuity equation for 2D geometries used here can be written as

$$\frac{\partial \rho}{\partial t} + \frac{\partial}{\partial x}(\rho v_x) + \frac{\partial}{\partial y}(\rho v_y) = 0. \tag{3.2}$$

Conservation of momentum in an inertial and non-accelerating reference frame is

$$\frac{\partial}{\partial t}(\rho \mathbf{v}) + \nabla \cdot (\rho \mathbf{v}\mathbf{v}) = -\nabla p + \nabla \cdot (\bar{\bar{\tau}}) + p\mathbf{g} + \mathbf{F} + S, \tag{3.3}$$

where p is the static pressure, $\bar{\bar{\tau}}$ is the stress tensor, $p\mathbf{g}$ is the gravitational body force, S is the source term (used for solidification equations in future sections), and $\mathbf{F}$ are the external body forces (which for these simulations is zero). The stress tensor is defined as

$$\bar{\bar{\tau}} = \mu\Big[(\nabla \mathbf{v} + \nabla \mathbf{v}^T) - \frac{2}{3}\nabla \cdot \mathbf{v} I\Big], \tag{3.4}$$

where μ is the molecular viscosity, I is the unit tensor, and the term on the right-hand side is the effect of volume dilation [6]. The classic second-order upwind scheme is used to solve for the momentum equations, along with a coupled scheme and PRESTO! to solve for the pressure. PRESTO! is a good scheme for this environment due to its strengths in modeling rotating flows [6].

3.3.1.2 Turbulence

Due to the relatively low viscosity and high density of liquid metals, flow is easily transitioned into the turbulent regime. Due to buoyancy-driven (in addition to Lorentz forces)

flow in VAR operation, the melt pool flow exhibits turbulence [5, 7, 10]. For this stage of the study I neglect Lorentz forces. The turbulence model selected for the numerical simulation is the standard k–ϵ model. Since being introduced by Launder and Spalding the standard k–ϵ model has seen widespread use in industry and academia. The highlighted benefits are its relatively low memory requirements, robustness, and reasonable accuracy. The standard k–ϵ is a two equation model consisting of the turbulent kinetic energy, k, and its rate of dissipation, ϵ.

The equation for the turbulent kinetic energy is

$$\frac{\partial}{\partial t}(\rho k) + \frac{\partial}{\partial x_i}(\rho k u_i) = \frac{\partial}{\partial x_j}\Big[\Big(\mu + \frac{\mu_t}{\sigma_k}\Big)\frac{\partial k}{\partial x_j}\Big] + G_k + G_b - \rho\epsilon + S, \tag{3.5}$$

where G_k is the rate of production of turbulent kinetic energy given by

$$G_k = \mu_t\Big(\frac{\partial u_j}{\partial x_i} + \frac{\partial u_i}{\partial x_j}\Big)\frac{\partial u_j}{\partial x_i}, \tag{3.6}$$

G_b is the generation of turbulence due to buoyancy given by

$$G_b = -g_i\frac{\mu_t}{\rho\sigma_h}\frac{\partial \rho}{\partial x_i}, \tag{3.7}$$

μ_t is the turbulent viscosity:

$$\mu_t = \rho C_\mu \frac{k^2}{\epsilon}. \tag{3.8}$$

The equation for the rate of dissipation is

$$\frac{\partial}{\partial t}(\rho\epsilon) + \frac{\partial}{\partial x_i}(\rho\epsilon u_i) = \frac{\partial}{\partial x_j}\Big[\Big(\mu + \frac{\mu_t}{\sigma_\epsilon}\Big)\frac{\partial \epsilon}{\partial x_j}\Big] + C_{1\epsilon}\frac{\epsilon}{k}\Big(G_k + C_{3\epsilon}G_b\Big) - C_{2\epsilon}\rho\frac{\epsilon^2}{k} + S \tag{3.9}$$

with the standard empirical constants used

$$C_{1\epsilon} = 1.44,\ C_{2\epsilon} = 1.92,\ C_\mu = 0.09,\ \sigma_k = 1.0,\ \sigma_\epsilon = 1.3 \tag{3.10}$$

3.3.1.3 Energy and solidification

The enthalpy-porosity technique is used in ANSYS Fluent for the modeling of solidification. This methodology uses liquid fraction, which assigns a value from 0 to 1 to each cell volume depending on what fraction of the cell domain is liquid. A cell with value of 1 is all liquid, and a cell with a value of 0 is completely solid. All cells that are not equal to 0 or 1 exactly consist of what is known as the mushy zone. The enthalpy-porosity technique treats the mushy zone as a pseudo porous medium, and uses an enthalpy balance to determine the liquid fraction. When a cell reaches a value of 0 (fully solid), the porosity will also reach zero [6].

The energy equation uses an enthalpy balance where the enthalpy of the material is calculated as the sum of the sensible enthalpy, h, and the latent heat, ΔH:

$$H = h + \Delta H, \tag{3.11}$$

where

$$h = h_{\text{ref}} + \int_{T}^{T_{\text{ref}}} c_p dT \tag{3.12}$$

and

$$\begin{aligned} h_{\text{ref}} &= \text{reference enthalpy} \\ T_{\text{ref}} &= \text{reference temperature} \\ c_p &= \text{specific heat at constant pressure} \end{aligned}$$

The latent heat content is described in terms of the latent heat of the material, L:

$$\Delta H = \beta L, \tag{3.13}$$

where β is the liquid fraction and can be defined as

$$\begin{aligned} &\beta = 0 \; if \; T < T_{\text{solidus}} \\ &\beta = 1 \; if \; T > T_{\text{liquidus}} \\ &\beta = \frac{T - T_{\text{solidus}}}{T_{\text{liquidus}} - T_{\text{solidus}}} \; if \; T_{\text{solidus}} < T < T_{\text{liquidus}} \end{aligned} \tag{3.14}$$

The energy equation is defined as

$$\frac{\partial}{\partial t}\Big(\rho H\Big) + \nabla \cdot \Big(\rho \mathbf{v} H\Big) = \nabla \cdot \Big(k \nabla T\Big) \tag{3.15}$$

Temperature is solved iteratively using the energy equation and the liquid fraction equation. The Voller and Prakash method is used to update the liquid fraction over the more traditional methods such as Voller and Swaminath due to T_{solidus} and T_{liquidus} being nearly equal for liquid metals [6].

3.3.1.4 Enthalpy-porosity and the momentum equation

The momentum equation is affected by the enthalpy-porosity technique through the addition of a source term, which takes into account the porosity of the medium. The porosity of each cell is equal to the liquid fraction of the cell, when the liquid fraction approaches zero, the porosity approaches zero, and therefore the velocity as well. The source (or sink) term is defined as

$$S = \frac{(1-\beta)^2}{(\beta^3 + \epsilon_0)} A_{\text{mush}} (\mathbf{v} - \mathbf{v}_p) \tag{3.16}$$

where ϵ_0 is a very small number to avoid dividing by zero, A_{mush} is the mushy zone constant (measures the amplitude of damping, high mushy zone constant leads to a more rapid transition of the velocity to zero as the material solidifies), and $\mathbf{v}_p$ is the pull velocity. The pull velocity will be discussed in further detail in the next section–but essentially the pull velocity for this scenario is equal to the melt rate of the electrode.

A sink term is also added to the turbulence equations

$$S = \frac{(1-\beta)^2}{(\beta^3 + \epsilon_0)} A_{\text{mush}} \phi \tag{3.17}$$

where ϕ is the turbulence quantity in question, (k and ϵ in this case). The energy equation is solved using a second order upwind scheme.

3.3.2 Boundary conditions, material properties, and meshing

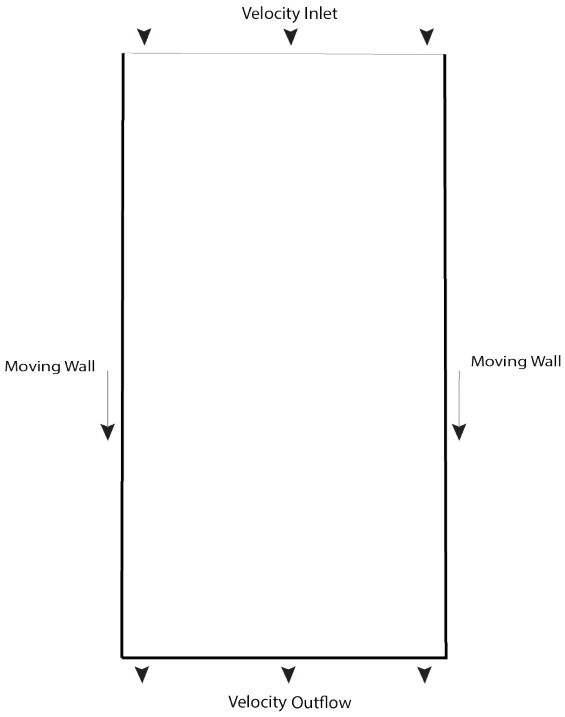

Figure 3.2: Fluid boundary conditions

The control volume in question consists of only the resultant ingot of the VAR process. The computational boundary conditions placed on the control volume are selected to represent the physical phenomena interacting with just the molten and solidifying metal.

For the fluid mechanics boundary conditions, the top of the ingot is a free surface, where material and energy are free to traverse. The fluid boundary condition selected is an inflow that equals the average melt rate of the process. In reality the electrode melt droplets are not uniform; however I assume an average inflow due to the much lower velocity of the droplets compared to melt pool velocities (10^{-5} m/s vs. 10^{-2} m/s, respectively) [5]. Along the sides (the crucible-ingot boundary), the fluid/solid translates at the velocity of the melt rate downward towards the outflow. The outflow is the pull velocity, which is also set as the melt rate. These boundary conditions are not exactly representative of the physical system, as in reality the ingot grows upwards as more

material stacks and solidifies on top of itself. However, for computational advantages I can change the reference frame to inspect only the melt pool, mushy zone, and some of the solidified ingot. So imagine the control volume moving upwards as the ingot grows during the melting process. This results in a quasi-steady-state solution to the solidification problem for relatively short periods of time, when an arc remains in one position for a small amount of time. This approach is valid for when the ingot has already grown past the initial phase of the process [5]. A diagram detailing the boundary conditions can be seen in Figure 3.2.

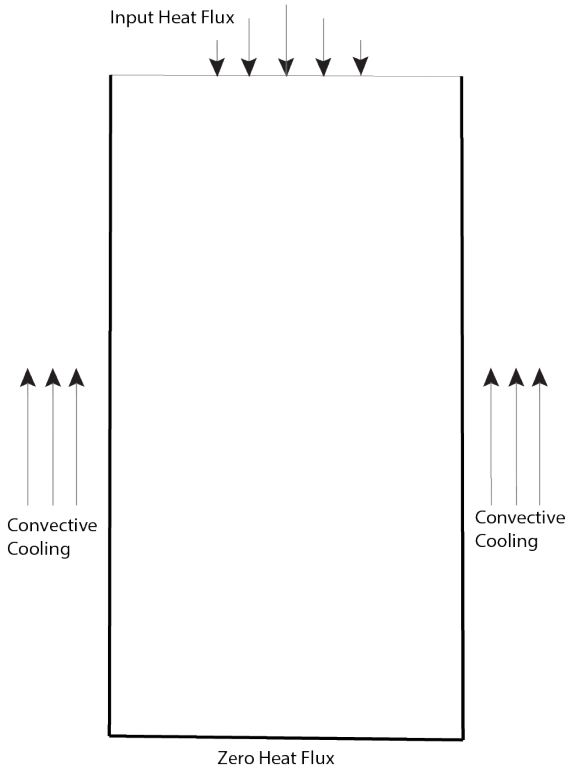

Figure 3.3: Thermal boundary conditions

As for the thermal boundary conditions, the top is an input heat flux of parabolic distribution located at the arc position. This heat flux is one of the biggest question marks in VAR process modeling, but for the purposes of this study approximations found from literature should be sufficient to determine effects on melt pool and solidification angle. The ingot-crucible interface is set to convective cooling, which is constant when

the ingot is in contact with the crucible, and offers relatively high heat coefficients. In reality the material shrink as it solidifies, leaving a gap of vacuum space between the ingot and the crucible. This negatively affects heat transfer; however, the shrinkage of the ingot will be neglected in this model. For future iterations and improvements this can be taken into account by applying variable heat transfer coefficient with respect to vertical position. This can be calculated as heat transfer between two bodies separated by a vacuum, mainly radiative heat transfer. The bottom surface is set to an outflow boundary condition, where conductive heat flux is zero, and the convective heat flux is unconstrained. [5]

The material selected is an uranium-niobium alloy. It was selected due to having a more shallow pool than other alloys like titanium, and the availability to find relevant material properties in the literature. Table 3.1 details the material properties used for the simulations. A linear dependance on temperature was added to the density.

Table 3.1: Material properties for the U-Nb alloy taken from Gartling et al. [5]

Material property	Value
Density	$1.56 \times 10^4\,\mathrm{kg/m^3}$
Specific heat	$200.0\,\mathrm{J/(kg\,K)}$
Thermal conductivity	$30.0\,\mathrm{J/(m\,s\,K)}$
Viscosity	$5.0 \times 10^{-3}\,\mathrm{kg/(m\,s)}$
Thermal expansion	$7.4 \times 10^{-5}\,\mathrm{/K}$
Latent heat	$8.0 \times 10^4\,\mathrm{J/kg}$
Liquidus temperature	$1605\,\mathrm{K}$
Solidus temperature	$1440\,\mathrm{K}$

The mesh is a standard quadrilateral 2D mesh with inflation on the ingot-crucible interface. The top and bottom boundaries are inlet and outlets, so inflation was added only on the wall interfaces to aid in boundary layer calculations; though wall effects should be minimal in this scenario due to very little fluid-wall contact area due to solidification. Ideally the melt pool and mushy zone are the only zones that require a fine mesh; however, the location and size of the zones is not always known beforehand. Due to the simulations not being too computationally expensive (less than 4 hours), the entire domain was given a mesh of maximum cell size of $2.5 \times 10^{-4}\,\mathrm{m}$. The diameter of the ingot is $0.3\,\mathrm{m}$ and a height of $0.5\,\mathrm{m}$. Ingots in reality are much taller, however for this pseudo steady-state

problem it is sufficient to look at just the top portion of the ingot.

3.4 Results and discussion

In order to study the effects of changing the arc position the melt pool will be studied by collecting data on its velocity, temperature, and liquid fraction profile. The arc was modeled as a parabolic heat flux at the top of the ingot. The simulation was initiated by solving for a centered arc until steady-state is achieved, then the arc was either moved 5 cm to the right, or remained in place. Data was collected after 5 physical seconds.

Figures 3.4 and 3.5 show contour plots of the liquid fraction for a centered arc position and an arc positioned 5 cm to the right of center. These results are after steady state was achieved and collected 5 seconds after the arc either remained centered or off-centered. These plots are only of the top part of the domain calculated. Qualitatively we observe that the solidification angle for the off-centered arc flattens out towards the side where the arc is positioned. Everything in between a liquid fraction of 1 and 0 is the mushy zone.

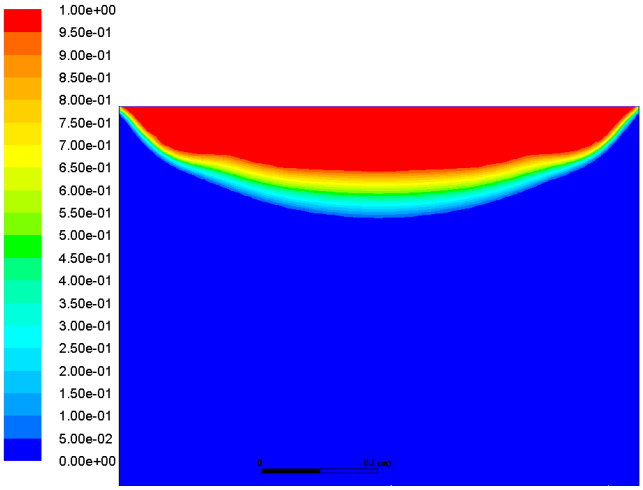

Figure 3.4: Liquid fraction for a centered arc position

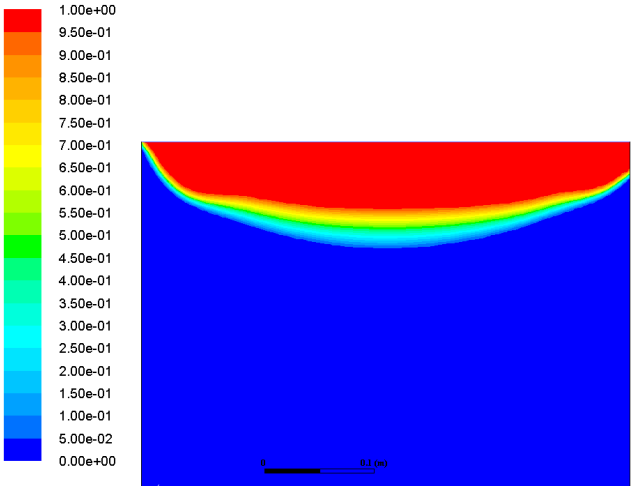

Figure 3.5: Liquid fraction for an arc position 5 cm right of the center

Figures 3.6 and 3.7 show the vector plots of the velocity magnitude in the melt pool for a centered and off-centered arc location. These values fall in line with literature where the melt pool velocities reach magnitudes on the order 10^{-2} m/s compared to the pull velocities in magnitude of 10^{-5} m/s [5]. Qualitatively we see a shift in the max velocity locations; for the centered arc, the max velocities occur on the bottom left and bottom right parts of the melt pool, while for the off-centered arc scenario the max velocities occur towards the crucible interface. Specifically on the side nearest the arc location. The velocity magnitude is also greater for the off-centered arc results, increasing by 25.9 %. This is occurring because the heat flux is causing more, hotter liquid metal to exist in contact with the crucible. There is a large temperature difference at the interface from the convective cooling applied to the crucible. Therefore, the liquid metal at the interface experiences more cooling, resulting in more rapid buoyancy changes.

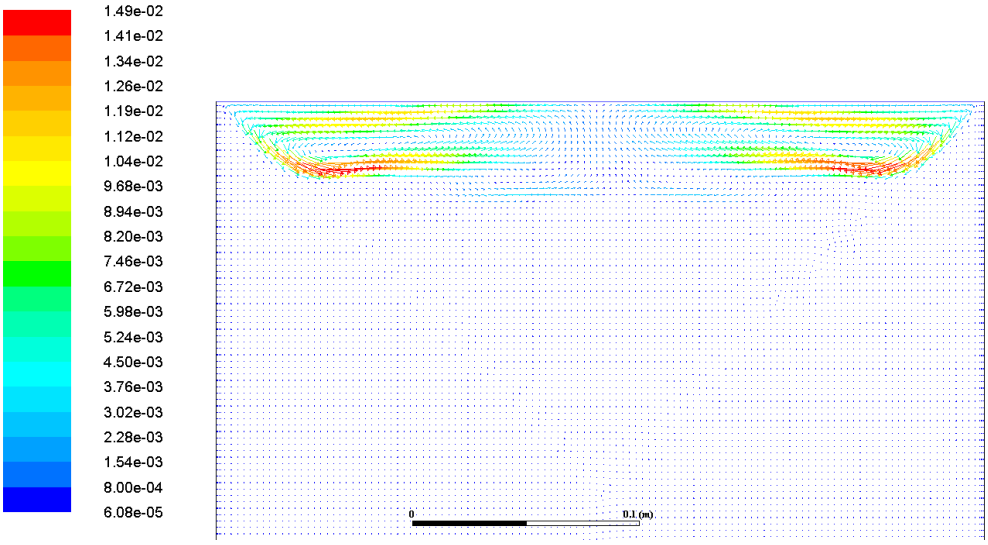

Figure 3.6: Velocity magnitude vector field for a centered arc location

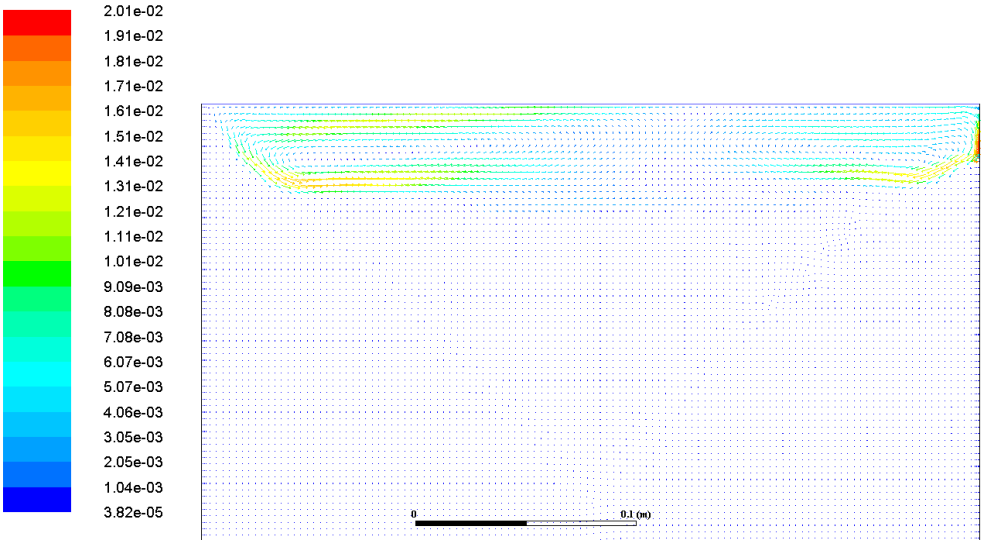

Figure 3.7: Velocity magnitude vector field for an off-centered arc location (arc located 5 cm right of center)

Figures 3.8 and 3.9 show plots of the velocity magnitude in the melt pool at varying

depths, for centered and off-centered arc locations respectively. The depths vary 2 cm, 3 cm, and 4 cm from the electrode-ingot gap. The maximum velocity at all depths increased for the off-center arc. The shallowest depth examined saw increases in velocity towards the side the arc was located, while depths below that show increases in velocity away from the arc location.

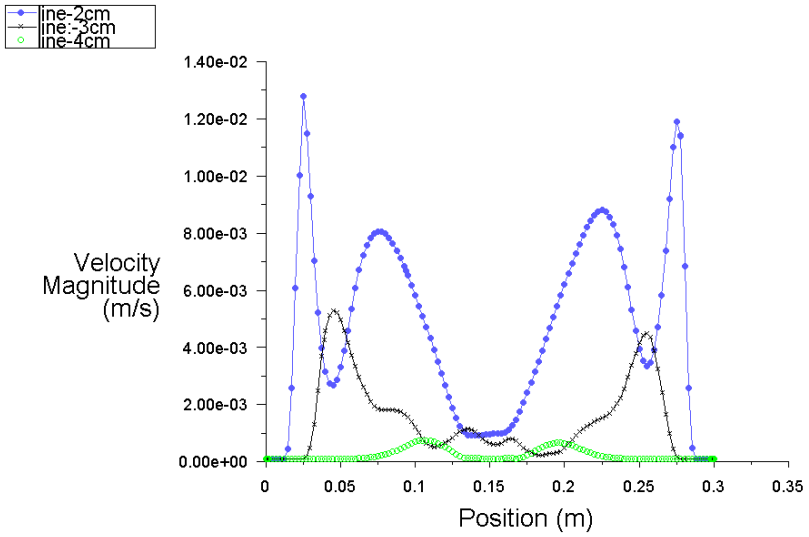

Figure 3.8: Velocity magnitude at different depths of the melt pool for a centered arc position

Figures 3.10 and 3.11 show plots of velocity magnitudes in the melt pool along the axial direction, for centered and off-centered arc locations respectively. They plot the velocities at the centerline and lines ± 0.075 m to the left and right. From these plots we can see the circulation patterns of the flow. Looking at the off-centered arc velocities the circulation appears stronger away from the arc location, comparing the quarter-line to the three-quarter-line data (the arc is located closer to the three-quarter-line). Velocity magnitudes on both sides of the circulation appear equal on both cases.

Figures 3.12 and 3.13 plot the temperature profiles in the melt pool at different depths. The depths vary from 2 cm, 3 cm, and 4 cm from the electrode-ingot gap. Figures 3.14 and 3.15 plot the temperature profiles in the melt pool for the centerline and ± 0.075 m to the left and right. The temperature profiles along the diameter of the ingot begin with a flat top near the electrode-ingot gap because of the circulation of the melt pool. As the

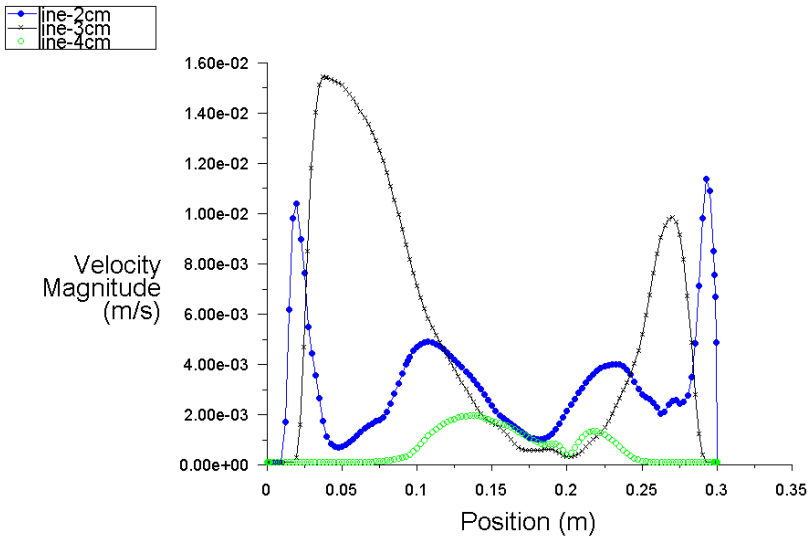

Figure 3.9: Velocity magnitude at different depths of the melt pool for an arc position 5 cm right of the center

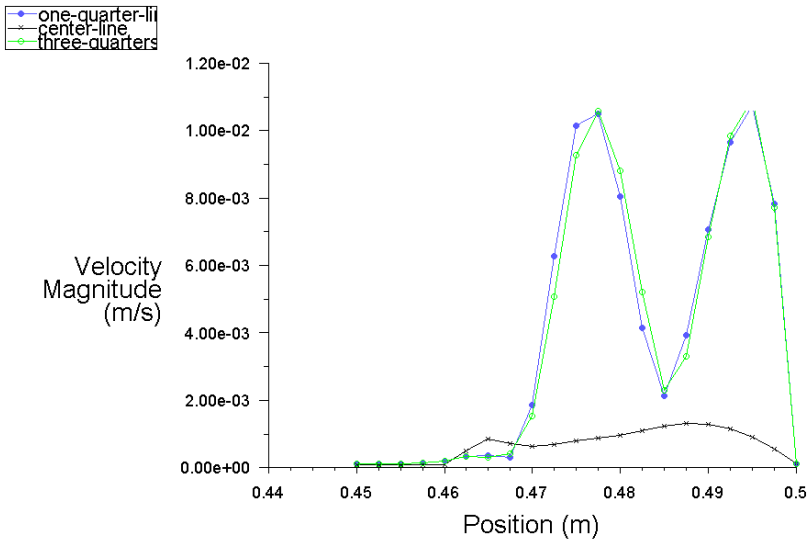

Figure 3.10: Velocity magnitude at different radial distances of the melt pool for a centered arc

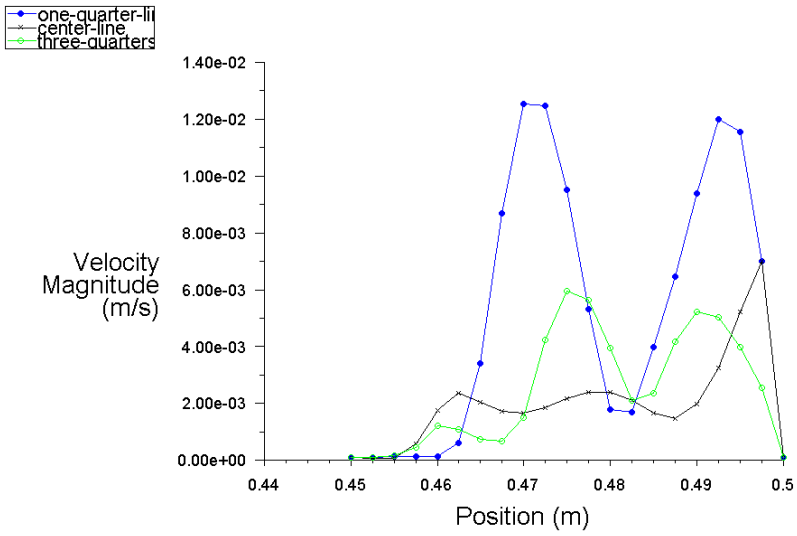

Figure 3.11: Velocity magnitude at different radial distances of the melt pool for an arc position 5 cm right of the center

depth decreases the profile becomes more parabolic, representing the melt pool shape. Off-centered arc temperature profiles are skewed towards the location of the arc.

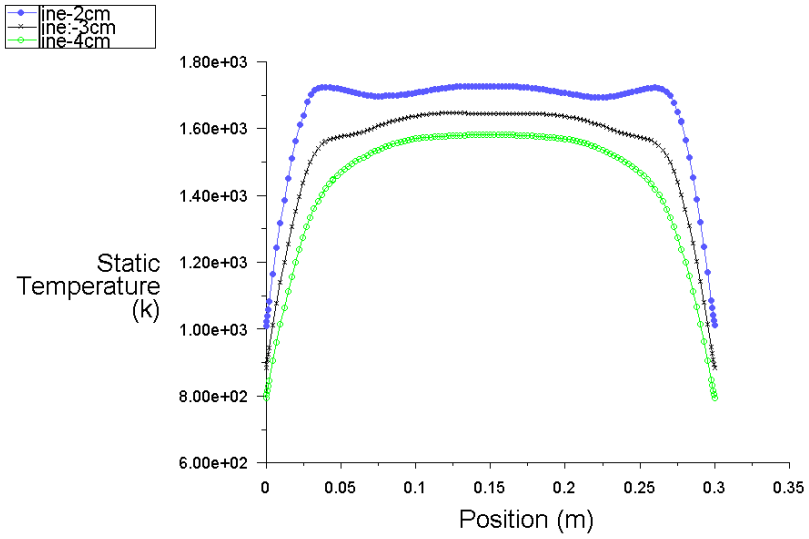

Figure 3.12: Temperature profiles at different depths of the melt pool for a centered arc

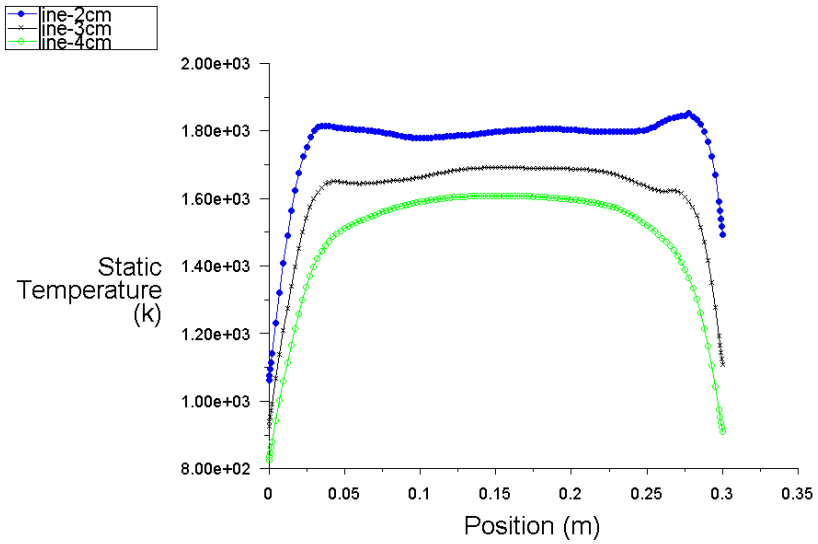

Figure 3.13: Temperature profiles at different depths of the melt pool for an arc position 5 cm right of the center

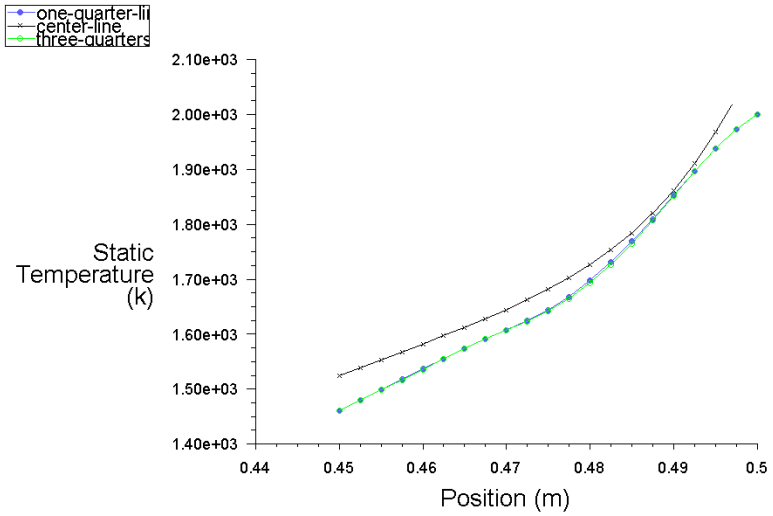

Figure 3.14: Temperature profiles at different radial distances of the melt pool for a centered arc

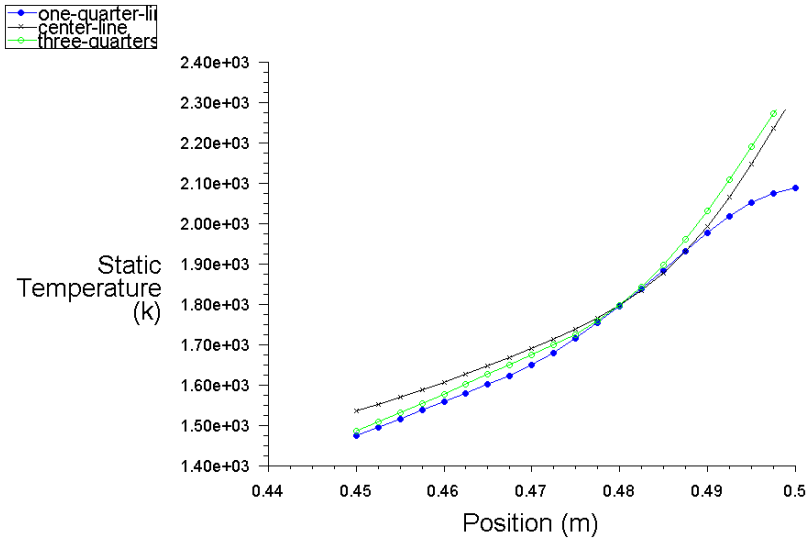

Figure 3.15: Temperature profiles at different radial distances of the melt pool for an arc position 5 cm right of the center

3.5 Conclusions

ANSYS Fluent was used to simulate a simplified vacuum arc remelting ingot solidification process. The model uses an enthalpy-porosity technique to calculate solidification of the liquid metal, it incorporates the turbulent flow of the melt pool using the two equation k–ϵ scheme, along with second-order upwind schemes for momentum and continuity. A coupled and PRESTO! techniques are used for pressure correction. The addition of magnetohydrodynamic effects is the next step towards developing an accurate model of the process. Simulations have shown sensitivity to the boundary conditions, so modeling has to be very furnace independent. To create a better model, extensive data is required about the boundary conditions of the specific furnace in question in order to validate results. Resources that were not available for my use. However, the data presented can be used as a comparative tool. Inspecting the difference between the data is useful information.

1. An arc located near the edge of the ingot, results a shallower solidification angle compared to a centered arc.

2. The model exhibited velocity magnitudes within literature bounds, while the melt pool velocities reach magnitudes of the order 10^{-2} m/s compared to the pull velocities in magnitude of 10^{-5} m/s [5].

3. A centered arc results in maximum liquid pool flow velocities located near the top and bottom of the circulating flow, while an off-centered arc leads to maximum velocity at the crucible interface. An off-centered arc increases flow velocities overall.

4. Liquid fraction increases in the direction of the arc location.

Chapter 4: Conclusions and future work

Vacuum arc remelting is a process that most people do not even know exists, yet it is a vital part of industries that affect their daily lives. It is a multi-billion dollar industry with roots in the state of Oregon. Even with its growth, many aspects of the process and physical phenomena are not completely solved. The process essentially involves melting of metal alloys through the application of high electrical currents. Input specimens, or electrodes, are inserted into the vacuum chamber of a furnace where they melt due to the formation of high electrical power arcs that form between it and the resultant ingot. This results in a high-quality metal alloy that exhibits high homogeneity both in microstructure and physically. Arc characteristics play a large role in determining ingot quality.

This work studied the role of arc location in two ways. First a sensitivity analysis of a developed arc position sensing technology was performed. The arc position sensing system is a combination of a finite element model, programming, and magnetic field measurements taken from furnaces using sensors. This thesis focused on the finite element model of the system: a magnetostatics simulation of a vacuum arc remelting furnace. It finds necessary furnace-specific constants for the arc position sensing algorithm. The main objective was to take a closer look at assumptions made in the model, and vary possible phenomena that could affect the accuracy of the system. The finite element software COMSOL Multiphysics was used to solve the magnetic field distribution of a representative VAR furnace. The overall accuracy of arc location predictions are shown sensitive to the furnace coefficients, so having a good model is vital. The model assumes a steady state approach, constant material properties, and no Joule heating. The assumptions studied include the vertical position of the sensor relative to the electrode-ingot gap, a varying electrode-ingot gap size, ingot shrinkage, and the use of multiple sensors rather than a single sensor. The arc position sensing technology works because arcs are a high concentration of current that creates a strong magnetic field, and that field can be used to deduce the location of arcs inside the furnace without intrusive instrumentation. Arcs are mainly vertical, so the magnetic field is most visible in a two-dimensional plane

perpendicular to the arc location. This leads to the loss of accuracy when the magnetic field sensors stray from the arc in the vertical direction. This can be solved by layering sensor rings vertically along a furnace. Using the results from the studies in this thesis, an estimate for the distance between the sensor rings can be made. This leads to another interesting problem: how to optimize the sensor distribution. Both this work and others in literature show diminishing returns when it comes to accuracy and total number of sensors in plane. This numerically is because the system is more accurate for sensors located closer to the arc location. When more than one sensor is introduced, there is more of a guarantee for an accurate prediction from one of the sensors. However, with more sensors, more less-accurate data is introduced into the averaging calculation. Perhaps a two-stage weighted average could produce better results than an unweighted average. Further possible future work involves the study of how the arc is modeled. Currently the arc is modeled as a small radius cylinder that distributes the current as a highly conductive solid, however an arcs electrical distribution is always changing and not representative of a small cylinder. This phenomena is very difficult to model, so accomplishing further research on this subject would be helpful to determine if it is necessary or not. The model assumes a perfect vacuum in the electrode-ingot gap, however in reality metal-vapor plasma is present in the electrode-arc gap. This alters the electronical characteristics of the area as well.

In addition to the studies on arc location predictions, a simplified solidification model was set up to analyze the effects of arc location on ingot solidification. The commercial software ANSYS Fluent 17.2 was used to model the physics using the control-volume method. The model neglected the magnetic effects on the liquid metal due to the electrical currents. This is an important parameter for this problem and is necessary for future work. The model also is a “pseudo” steady state assumption, as it does not solve for the entire process and the ingot growth. An extensive amount of validation is needed to use the model outright. Optimally, the model should be specialized for a specific furnace, whose data can be collected regarding the heat transfer coefficients due to convective cooling and heat flux inserted at the top boundary. Thermal boundary conditions at the crucible interface were assumed to be constant. The convective cooling should be a function that better represents the water cooling system, which varies as the water increases in temperature as it cools the crucible. Contact from the ingot to the crucible is also not constant, as the ingot shrinks when it cools contact is lost, directly affecting the

cooling due to the loss of conduction heat transfer at the interface. Validation is necessary for future work. However, this model suffices to study the effects of arc location on the melt pool and its solidification. Results from the velocity profile of the pool are within the same magnitude as published in literature by authors who made the same approach. Overall it is a useful first step towards building a solidification model. Future steps include expanding from a two-dimensional analysis to a fully three-dimensional analysis. Getting a 3D model that incorporates magnetohydrodynamics as well for a moving arc would lead to interesting data that could potentially be useful to the industry.

Bibliography

[1] ANSYS Inc. ANSYS Fluent. v17.2, 2016.

[2] Joseph J Beaman, Luis Felipe Lopez, and Rodney L Williamson. Modeling of the vacuum arc remelting process for estimation and control of the liquid pool profile. *J. Dyn. Sys., Meas., Control*, 136(3):031007–11, May 2014.

[3] L A Bertram, P R Schunk, S N Kempka, F Spadafora, and R Minisandram. The macroscale simulation of remelting processes. *JOM*, 50(3):18–21, March 1998.

[4] COMSOL Inc. COMSOL Multiphysics. 4.3b, May 2013.

[5] D K Gartling and P A Sackinger. Finite element simulation of vacuum arc remelting. *Int. J. Numer. Methods Fluids*, 24(12):1271–1289, June 1997.

[6] ANSYS Inc. Fluent theory guide. 17.2, 2016.

[7] Kanchan M Kelkar, Suhas V Patankar, Alec Mitchell, Osamu Kanou, Nobuo Fukada, and Kenji Suzuki. Computational modeling of the Vacuum Arc Remelting (VAR) process used for the production of ingots of Titanium alloys. *11th World Conference on Titanium*, June 2007.

[8] Hafid El Mir, Alain Jardy, Jean-Pierre Bellot, Pierre Chapelle, David Lasalmonie, and Jean Senevat. Thermal behaviour of the consumable electrode in the vacuum arc remelting process. *Journal of Materials Processing Technology*, 210(3):564–572, February 2010.

[9] Bindu G Nair and R M Ward. An analysis of the use of magnetic source tomography to measure the spatial distribution of electric current during vacuum arc remelting. *Meas. Sci. Technol.*, 20(4):045701–12, February 2009.

[10] Koulis Pericleous, Georgi Djambazov, Mark Ward, Lang Yuan, and Peter D Lee. A multiscale 3D model of the vacuum arc remelting process. *Metall and Mat Trans A*, 44(12):5365–5376, March 2013.

[11] G Reiter, V Maronnier, C Sommitsch, M Gäumann, W Schützenhöfer, and R Schneider. Numerical simulation of the VAR process with calcosoft®-2D and its validation. In *LMPC 2003*, pages 77–86, Nancy, France, September 2003.

[12] James A Van Den Avyle, John A Brooks, and Adam C Powell. Reducing defects in remelting processes for high-performance alloys. *JOM*, pages 22–26, mar 1998.

[13] Lijun Wang, Shenli Jia, Zongqian Shi, and Mingzhe Rong. Numerical simulation of vacuum arc under different axial magnetic fields. *J. Phys. D: Appl. Phys.*, 38(7):1034–1041, March 2005.

[14] C Rigel Woodside and Paul E King. A measurement system for determining the positions of arcs during Vacuum arc remelting. In *2010 IEEE Instrumentation & Measurement Technology Conference Proceedings*, pages 452–457. IEEE, March 2010.

[15] C Rigel Woodside, Paul E King, and Chris Nordlund. Arc distribution during the vacuum arc remelting of Ti-6Al-4V. *Metall and Materi Trans B*, 44(1):154–165, February 2013.

[16] Zhi-jun Yang, Xiao-hua Zhao, Hong-chao Kou, Jin-shan Li, Rui Hu, and Lian Zhuo. Numerical simulation of temperature distribution and heat transfer during solidification of titanium alloy ingots in vacuum arc remelting process. *Transactions of Nonferrous Metals Society of China*, 20(10):1957–1962, October 2010.

[17] K O Yu. *Modelling for Casting and Solidification Processing.* Dekker, 2002.

[18] F J Zanner, C Adasczik, T O'Brien, and L A Bertram. Observations of melt rate as a function of arc power, CO pressure, and electrode gap during vacuum consumable arc remelting of Inconel 718. *Metallurgical Transactions B*, 15(1):117–125, 1984.

[19] FJ Zanner, RJ Williamson, and RP Harrison. Vacuum arc remelting of alloy 718. *The Minerals, Metals & Materials Society*, 1989.

[20] Xiao-hua Zhao, Jin-shan Li, Zhi-jun Yang, Hong-chao Kou, Rui Hu, and Lian Zhou. Numerical simulation of fluid flow caused by buoyancy forces during vacuum arc remelting process. *J. Shanghai Jiaotong Univ. (Sci.)*, 16(3):272–276, June 2011.

APPENDICES

Appendix A: APS study scripts

The following are Matlab scripts used to import the data from the model and calculate arc position predictions. It's also used for the plotting of results. The first script is used for arc location predictions using one sensor, and to display general values such as the magnetic field values in the furnace. The second script is what is used to calculate arc locations using four sensors. All data collected are basically different variations of these. For studies such as the sensor height problem, the scripts were added into a loop with other minor changes.

A.1 One sensor:

```
clear
clc
clf

%% Import Data
Bex = importdata('E:\COMSOL\DataFiles\DomainStudy\2meter\Bex120extrafine.txt
Bx = Bex(:,2);                % Magnetic Flux Density x-comp [T]
Bey = importdata('E:\COMSOL\DataFiles\DomainStudy\2meter\Bey120custom.txt')
By = Bey(:,2);                % Magnetic Flux Density y-comp [T]
B = (Bx.^2+By.^2).^(1/2);
theta0 = Bex(:,1);
theta0d = theta0*180/pi;

%% Inputs
I = 35000;                    % Current [Amps]
f0 = 1;                       % Arc number coefficient
r = (0.05:0.32/4:0.37);         % Distance form center of furnace to arc [m]
N = length(Bx)./length(r);
```

```
%% Finding Theta
R0 = kron(r,ones(1,N));      % Repeater for radius numbers
R = rot90(R0,3);             % Rotation of Matrix for future operations
rs = 0.64;                   % Distance from sensor to center of furnace [m]
theta1 = theta0+pi/2;        % Input theta in COMSOL model. Arc angular posi
h = sin(theta1).*R;          % Height of arc-center-sensor triangle [m]
% Gemoetry Calculations
b = cos(theta1).*R;          % [m]
a = rs - b;                  % [m]
d = (a.^2 + h.^2).^(1/2);    % [m]
gamma = atan(h./a);          % [rad]
theta = (pi/2) - gamma;      % Angle of arc from sensor [rad]
thetad = theta*180/pi;

%% Cartesian Positioning

x = R.*cos(theta0);
y = R.*sin(theta0);

%% Furnace Coefficients
% Regression fit

mt0 = 9e-8;
et = @(mt)sum((Bx - mt*I*(((f0*sin(theta))./d)-(1./rs))).^2);
eti = fminsearch(et,mt0, optimset('TolX',1e-10));

mr0 = 9e-8;
er = @(mr)sum(((By - mr*I*(((-f0*cos(theta))./d))).^2));
eri = fminsearch(er,mr0,optimset('TolX',1e-10));

xdata = [theta,d];
ydatax = Bx;
```

```
ydatay = By;
[mt,resnormx] = lsqcurvefit(@(mx,xdata)mx*I*((sin(xdata(:,1))./xdata(:,2))-
[mr,resnormy] = lsqcurvefit(@(my,xdata)my*I*((-cos(xdata(:,1))./xdata(:,2)))

cftool

%% Arc Position Determination

mrr = 9e-8;
mtr = 4.9e-8;

df = (I*mr*mt)./(((I^2*mr^2*mt^2)/(rs^2) + (2.*I.*Bx.*mt.*mr^2)./rs + By.^2
thetaf = acos(-By.*d./(mr*I));

dfr = (I*mrr*mtr)./(((I^2*mrr^2*mtr^2)/(rs^2) + (2.*I.*Bx.*mtr.*mrr^2)./rs +
thetafr = acos(-By.*d./(mrr*I));

figure(1)
plot(thetaf,df,'*')
hold on; grid on;
title('Data from FEM');
xlabel('Angle from sensor [rad]');ylabel('Distance from sensor [m]')

figure(2)
plot(theta,d,'*')
hold on; grid on;
title('Input Values');
xlabel('Angle from sensor [rad]');ylabel('Distance from sensor [m]')

figure(3)
plot(thetafr,dfr,'*')
hold on; grid on;
title('With Expected (Rigels) Coefficients');
```

```
xlabel('Angle from sensor [rad]');ylabel('Distance from sensor [m]')

for i = 1:3

    mrz = [7e-8:1e-8:9e-8]
    mtz = [7e-8:-1e-8:5e-8]
    dfz = (I*mrz(i)*mtz(i))./(((I^2*mrz(i)^2*mtz(i)^2)/(rs^2) + (2.*I.*Bx.*
    thetafz = acos(-By.*d./(mrz(i)*I));
    figure(4)
    plot(thetafz,dfz,'*')
    legend('Mr = 7e-8, Mt = 7e-8','Mr = 8e-8, Mt = 6e-8','Mr = 9e-8, Mt = 5
    title('Furnace Coefficient Sensitivity')
    xlabel('Angle from sensor [rad]');ylabel('Distance from sensor [m]')
    hold on; grid on;

end

% ed = 100*abs(dfr-df)./df;
% eth = 100*abs(thetafr-thetaf)./thetaf;

rpos = (thetafr.^2+dfr.^2).^(1/2);
mpos = (thetaf.^2+df.^2).^(1/2);

epos = 100*(abs(rpos-mpos)./mpos);

figure(8)
scatter3(theta,d,epos)
title('Percent Positional Error Between Current Model and Expected Results'
xlabel('Angle from sensor (theta)[rad]');ylabel('Distance from sensor (d)[m

%% Plotting

figure(5)
```

```
scatter3(x,y,B)
xlabel('x');ylabel('y');zlabel('Bnorm Magnetic Flux Density');
hold on; grid on;

figure(6)
x1 = (-0.5:0.05:0.5);
y1 = (-0.5:0.05:0.5);
[X,Y] = meshgrid(x1,y1);
Z = griddata(x,y,B,X,Y);
mesh(X,Y,Z)
xlabel('x [m]');ylabel('y [m]');zlabel('Bnorm Magnetic Flux Density');
hold on; grid on;

figure(7)
plot(theta0d,thetad,'*')
hold on; grid on;
xlabel('Input Theta');ylabel('Sensor Theta');
```

A.2 Multiple sensors:

```
clear
clc
close all

%% Import Data
%Sensor Position (0,-0.64)
Bex0 = importdata('E:\COMSOL\DataFiles\SymmetryStudy\Bet120customA.txt');
Bx0 = Bex0(:,2);                % Magnetic Flux Density x-comp [T]
Bey0 = importdata('E:\COMSOL\DataFiles\SymmetryStudy\Ber120customA.txt');
By0 = Bey0(:,2);                % Magnetic Flux Density y-comp [T]
B0 = (Bx0.^2+By0.^2).^(1/2);
thetai = Bex0(:,1);
thetad = thetai*180/pi;
```

```
%Sensor Position (0.64,0)
Bex1 = importdata('E:\COMSOL\DataFiles\SymmetryStudy\Bet120customB.txt');
Bx1 = Bex1(:,2);                % Magnetic Flux Density x-comp [T]
Bey1 = importdata('E:\COMSOL\DataFiles\SymmetryStudy\Ber120customB.txt');
By1 = Bey1(:,2);                % Magnetic Flux Density y-comp [T]
B1 = (Bx1.^2+By1.^2).^(1/2);

%Sensor Position (0,0.64)
Bex2 = importdata('E:\COMSOL\DataFiles\SymmetryStudy\Bet120customC.txt');
Bx2 = -Bex2(:,2);                % Magnetic Flux Density x-comp [T]
Bey2 = importdata('E:\COMSOL\DataFiles\SymmetryStudy\Ber120customC.txt');
By2 = -Bey2(:,2);                % Magnetic Flux Density y-comp [T]
B2 = (Bx2.^2+By2.^2).^(1/2);

%Sensor Position (-0.64.0)
Bex3 = importdata('E:\COMSOL\DataFiles\SymmetryStudy\Bet120customD.txt');
Bx3 = -Bex3(:,2);                % Magnetic Flux Density x-comp [T]
Bey3 = importdata('E:\COMSOL\DataFiles\SymmetryStudy\Ber120customD.txt');
By3 = Bey3(:,2);                % Magnetic Flux Density y-comp [T]
B3 = (Bx3.^2+By3.^2).^(1/2);


%% Inputs
I = 35000;                      % Current [Amps]
f0 = 1;                         % Arc number coefficient
r = (0.05:0.32/6:0.37);           % Distance form center of furnace to arc [m]
N = length(Bx0)./length(r);

%% Finding Theta
R0 = kron(r,ones(1,N));         % Repeater for radius numbers
R = rot90(R0,3);                % Rotation of Matrix for future operations
rs = 0.64;                      % Distance from sensor to center of furnace [m]
```

```
theta0 = thetai;        % Input theta in COMSOL model. Arc angular position
h0 = cos(theta0).*R;          % Height of arc-center-sensor triangle [m]
% Gemoetry Calculations
b0 = sin(theta0).*R;          % [m]
a0 = rs - b0;                  % [m]
d0 = a0+b0;    % [m]
gamma0 = atan(h0./a0);          % [rad]
theta0 = pi/2 - gamma0;      % Angle of arc from sensor [rad]
thetad0 = theta0*180/pi;

theta1 = thetai;        % Input theta in COMSOL model. Arc angular position
h1 = sin(theta1).*R;          % Height of arc-center-sensor triangle [m]
% Gemoetry Calculations
b1 = cos(theta1).*R;          % [m]
a1 = rs - b1;                  % [m]
d1 = (a1.^2 + h1.^2).^(1/2);    % [m]
gamma1 = atan(h1./a1);          % [rad]
theta1 = (pi/2) - gamma1;      % Angle of arc from sensor [rad]
thetad1 = theta1*180/pi;

theta2 = pi/2 - thetai;        % Input theta in COMSOL model. Arc angular po
h2 = sin(theta2).*R;          % Height of arc-center-sensor triangle [m]
% Gemoetry Calculations
b2 = cos(theta2).*R;          % [m]
a2 = rs - b2;                  % [m]
d2 = (a2.^2 + h2.^2).^(1/2);    % [m]
gamma2 = atan(h2./a2);          % [rad]
theta2 = (pi/2) + gamma2;      % Angle of arc from sensor [rad]
thetad2 = theta2*180/pi;

theta3 = thetai+pi;        % Input theta in COMSOL model. Arc angular positio
h3 = sin(theta3).*R;          % Height of arc-center-sensor triangle [m]
```

```
% Gemoetry Calculations
b3 = cos(theta3).*R;            % [m]
a3 = rs - b3;                    % [m]
d3 = (a3.^2 + h3.^2).^(1/2);     % [m]
gamma3 = atan(h3./a3);           % [rad]
theta3 = (pi/2) - gamma3;        % Angle of arc from sensor [rad]
thetad3 = theta3*180/pi;

%% Cartesian Positioning

x = R.*cos(thetai);
y = R.*sin(thetai);

%% Furnace Coefficients
% Regression fit
xdata = [theta0,d0];

ydatax0 = Bx0;
ydatay0 = By0;
[mt0,resnormx0] = lsqcurvefit(@(mx,xdata)mx*I*((sin(xdata(:,1))./xdata(:,2))
[mr0,resnormy0] = lsqcurvefit(@(my,xdata)my*I*((-cos(xdata(:,1))./xdata(:,2

ydatax1 = Bx1;
ydatay1 = By1;
[mt1,resnormx1] = lsqcurvefit(@(mx,xdata)mx*I*((sin(xdata(:,1))./xdata(:,2))
[mr1,resnormy1] = lsqcurvefit(@(my,xdata)my*I*((-cos(xdata(:,1))./xdata(:,2

ydatax2 = Bx2;
ydatay2 = By2;
[mt2,resnormx2] = lsqcurvefit(@(mx,xdata)mx*I*((sin(xdata(:,1))./xdata(:,2))
[mr2,resnormy2] = lsqcurvefit(@(my,xdata)my*I*((-cos(xdata(:,1))./xdata(:,2

ydatax3 = Bx3;
```

```
ydatay3 = By3;
[mt3,resnormx3] = lsqcurvefit(@(mx,xdata)mx*I*((sin(xdata(:,1))./xdata(:,2))
[mr3,resnormy3] = lsqcurvefit(@(my,xdata)my*I*((-cos(xdata(:,1))./xdata(:,2


%% Arc Position Determination
mrr = 9e-8;
mtr = 4.9e-8;

df0 = (I*mr0*mt0)./(((I^2*mr0^2*mt0^2)/(rs^2) + (2.*I.*Bx0.*mt0.*mr0^2)./rs
thetaf0 = acos(-By0.*df0./(mr0*I));

df1 = (I*mr1*mt1)./(((I^2*mr1^2*mt1^2)/(rs^2) + (2.*I.*Bx1.*mt1.*mr1^2)./rs
thetaf1 = acos(-By1.*df1./(mr1*I));

df2 = (I*mr2*mt2)./(((I^2*mr2^2*mt2^2)/(rs^2) + (2.*I.*Bx2.*mt2.*mr2^2)./rs
thetaf2 = acos(-By2.*df2./(mr2*I));

df3 = (I*mr3*mt3)./(((I^2*mr3^2*mt3^2)/(rs^2) + (2.*I.*Bx3.*mt3.*mr3^2)./rs
thetaf3 = acos(-By3.*df3./(mr3*I));

dfr = (I*mrr*mtr)./(((I^2*mrr^2*mtr^2)/(rs^2) + (2.*I.*Bx0.*mtr.*mrr^2)./rs
thetafr = acos(-By0.*dfr./(mrr*I));


%% Conversion

xf0 = df0.*cos(thetaf0);
yf0 = df0.*sin(thetaf0);

xf1 = df1.*cos(thetaf1);
yf1 = df1.*sin(thetaf1);
```

```
xf2 = df2.*cos(thetaf2);
yf2 = df2.*sin(thetaf2);

xf3 = df3.*cos(thetaf3);
yf3 = df3.*sin(thetaf3);

xfr = dfr.*cos(thetafr);
yfr = dfr.*sin(thetafr);

xff = d0.*cos(theta0);
yff = d0.*sin(theta0);

%% Error

rpos = (xfr.^2+yfr.^2).^(1/2);
mpos0 = (xf0.^2+yf0.^2).^(1/2);
mpos1 = (xf1.^2+yf1.^2).^(1/2);
mpos2 = (xf2.^2+yf2.^2).^(1/2);
mpos3 = (xf3.^2+yf3.^2).^(1/2);
eposr = (xff.^2+yff.^2).^(1/2);

epos0 = 100*((abs(rpos-mpos0))./mpos0);
epos1 = 100*((abs(rpos-mpos1))./mpos1);
epos2 = 100*((abs(rpos-mpos2))./mpos2);
epos3 = 100*((abs(rpos-mpos3))./mpos3);

epose0 = 100*((abs(eposr-mpos0))./mpos0);
epose1 = 100*((abs(eposr-mpos1))./mpos1);
epose2 = 100*((abs(eposr-mpos2))./mpos2);
epose3 = 100*((abs(eposr-mpos3))./mpos3);

eposave0 = sum(epos0)./120;
eposave1 = sum(epos1)./120;
```

```
eposave2 = sum(epos2)./120;
eposave3 = sum(epos3)./120;

eposaver = sum(epose0)./120;

%% Plotting

figure(1)
x1 = (-0.5:0.05:0.5);
y1 = (-0.5:0.05:0.5);
[X,Y] = meshgrid(x1,y1);
Z = griddata(x,y,B0,X,Y);
mesh(X,Y,Z)
xlabel('x [m]');ylabel('y [m]');zlabel('Bnorm Magnetic Flux Density');
hold on; grid on;

figure(2)
scatter(xf0,yf0)
hold on; grid on;
scatter(xff,yff)
legend('FEM','Exact')
xlabel('x [m]');ylabel('y [m]');

figure(3)
scatter3(xff,yff,epos0)
title('Percent Positional Error Between Current Model and Expected Results'
xlabel('x [m]');ylabel('y [m]')

figure(4)
x2 = (-0.5:0.05:0.5);
y2 = (-0.5:0.05:0.5);
[X1,Y1] = meshgrid(x2,y2);
Z2 = griddata(x,y,epose0,X1,Y1);
```

```
mesh(X1,Y1,Z2)
title('Percent Positional Error');
xlabel('x [m]');ylabel('y [m]')

figure(5)
plot(thetad,thetad0)
grid on; hold on;
plot(thetad,thetad1)
plot(thetad,thetad2)
plot(thetad,thetad3)
legend('0','1','2','3')
xlabel('input theta');ylabel('theta')
```